Petroleum Science 23 (2026) 1197–1219

Contents lists available at ScienceDirect

Petroleum Science

journal homepage: www.keaipublishing.com/en/journals/petroleum-science

Original Paper

Numerical and physical simulations of acoustic imaging for adjacent well detection while drilling

Teng Zhao, Gen-Sheng Li *, Xiao-Hua Che, Wen-Xiao Qiao, Jun-Qiang Lu, Bai-Yong Men

State Key Laboratory of Petroleum Resources and Engineering, China University of Petroleum (Beijing), Beijing, 102249, China

A R T I C L E I N F O

Article history:
Received 4 July 2025
Received in revised form
19 August 2025
Accepted 27 October 2025
Available online 1 November 2025

Edited by Meng-Jiao Zhou

Keywords:
Adjacent well detection
Acoustic logging while drilling
Compressed sensing
Numerical simulation
Physical simulation

A B S T R A C T

With increase in the number of operations involving relief wells, radial wells, U-shaped wells, and other complex well structures, challenges such as collision prevention, obstacle bypassing, and adjacent-well connectivity achievement during drilling have become inevitable. These challenges necessitate a technology that can accurately detect adjacent wells in real time during drilling operations. As current borehole acoustic reflection imaging technology heavily relies on cable-based logging, it cannot perform real-time detection of adjacent wells during drilling, thereby limiting the drilling efficiency. This study proposes a new adjacent-well-acoustic-detection-while-drilling method that integrates wireline borehole acoustic reflection imaging with drilling technology, along with an adjacent-well imaging method based on compressed sensing (CS). Together, these methods enable high-resolution, real-time detection of the adjacent target wells during drilling, ensuring safe and efficient underground drilling operations. The finite-difference method was used to simulate three-dimensional numerical models under drilling conditions for two scenarios—with and without target wells adjacent to the drilling well. Experimental validation was conducted in a water tank using an adjacent-well-acoustic-detection-while-drilling tool. The simulated target well was imaged using the CS method, and the imaging results were compared with those obtained from numerical and physical simulations, thereby validating the feasibility of the proposed acoustic detection and imaging methods. The results demonstrate that as the radial distance from the target well increases, the PP echo exhibits delayed arrival times and approaches a plane wave while exhibiting amplitude attenuation. Conversely, a linear increase in the target well diameter advances the PP echo arrival time and enhances its amplitude proportionally. When the target and drilling wells are approximately parallel with a small intersection angle, PP echoes yield better detection results than SS echoes; when the wells are coplanar with a large intersection angle, SS echoes provide better detection results. The receiver element aligned with the target well's azimuth detects all echo modes with the earliest arrival times and highest amplitudes. The adjacent-well imaging method based on CS offers very high spatial resolution, with target wells appearing as local amplitude maxima. This feature enables the precise determination of their azimuth and inclination relative to the drilling wells. The findings offer a solid physical and methodological foundation for real-time detection of adjacent wells during drilling operations and demonstrate enormous theoretical and engineering application potential.

© 2026 Publishing services by Elsevier B.V. on behalf of KeAi Communications Co. Ltd. This is an open access article under the CC BY-NC-ND license (http://creativecommons.org/licenses/by-nc-nd/4.0/).

1. Introduction

In petroleum engineering, horizontal wells, cluster wells, and infilling wells are used to extract shale oil and gas, as well as oil and gas from low-permeability, tight reservoirs. Relief wells are used to extinguish oil and gas well fires or control blowout incidents that occur during offshore or onshore drilling operations. Radial wells enlarge geothermal reservoirs contact and may be hydraulically fractured to expand the area of effective reservoir stimulation. U-shaped wells enable the effective extraction of geothermal heat from medium-depth reservoirs, and multibranch radial wells support the economical and efficient development of natural gas hydrates (Al-Muhailan et al., 2014; Varela et al., 2015; Li et al., 2022a, 2022b; Song et al., 2022; Wang et al., 2024). The growing use of relief wells, radial wells, U-shaped wells, and other

---

* Corresponding author.
E-mail address: ligs@cup.edu.cn (G.-S. Li).
Peer review under the responsibility of China University of Petroleum (Beijing).

https://doi.org/10.1016/j.petsci.2025.10.027

1995-8226/© 2026 Publishing services by Elsevier B.V. on behalf of KeAi Communications Co. Ltd. This is an open access article under the CC BY-NC-ND license (http://creativecommons.org/licenses/by-nc-nd/4.0/).

complex well structures has led to challenges such as collision prevention (avoidance of unintentional contact between the newly drilled wellbore and nearby existing wells), obstacle avoidance (avoidance of downhole obstructions such as casing, plugs, or geological anomalies during drilling), and adjacent-well connectivity achievement during drilling operations. When drilling new wells under complex well conditions, safe drilling decisions rely on the real-time measurements of distance and azimuth for the well being drilled (the measurement well) relative to the existing wells (target wells).

Existing adjacent-well detection methods primarily fall into two categories: electromagnetic and acoustic detection methods. Electromagnetic detection methods include passive and active measurement modes. In passive electromagnetic detection, the position of the target well is determined by measuring abnormal interference magnetic fields superimposed on the underground geomagnetic field. This method heavily relies on the residual magnetism of metallic materials present in the target well, limiting its effective detection range and accuracy. In particular, effective detection operations cannot be performed if multiple magnetic interference sources exist in the formation (Lane and Wesson, 1992; Hanak and Estes, 2015). Active electromagnetic detection uses magnetic sources such as a permanent-magnet short sections, energized solenoids, or electrified pipe strings to extend the measurement range and achieve high precision (Wang et al., 2019, 2020, 2022). However, active electromagnetic detection tools, which generate magnetic fields using either permanent-magnet short sections or energized solenoids, must be deployed in the measurement and target wells, complicating the operation and disrupting normal oil and gas production in the target well (Kuckes et al., 1996; Grills, 2002). Moreover, electromagnetic detection tools cannot be lowered into a well experiencing a blowout (hereafter referred to as the accident well) during interconnecting operations with a relief well. In such cases, directional drilling must be performed using a Wellspot-series tool (Zhang et al., 2020; Gao et al., 2023). This tool locates the adjacent well by transmitting current into the formation and detecting the magnetic field generated in the casing of the accident well; however, its effectiveness is limited to cases where the accident well is cased.

Acoustic detection methods deploy acoustic logging tools in measurement wells. During logging, the considered tool emits acoustic energy into the formation surrounding the well and receives scattered echo waveforms from the target well. The target well location is determined based on the arrival time and amplitude of these echo waveforms. This method does not require the tool to be lowered into the target well, thereby enhancing safety, lowering operational costs, and making it applicable to open- and cased-hole scenarios. Acoustic detection methods include borehole monopole, dipole, and azimuthal acoustic reflection imaging methods. The borehole monopole acoustic reflection imaging method uses monopole acoustic sources and receivers to detect the distance to the target well, but it has difficulty determining the azimuth (Hornby, 1989; Chai et al., 2009). The borehole dipole acoustic reflection imaging method utilizes dipole acoustic sources and receivers, enabling detection of the distance to the target well and offering a limited ability to determine its azimuth. This method is widely applied in oilfields (Tang, 2004; Su et al., 2014; Tang et al., 2016; Gu et al., 2021; Li et al., 2022c, 2022d; Niu and Su, 2022; Zhao et al., 2024a, 2024b; Kong et al., 2024; Liu et al., 2025; Gu et al., 2025). However, this method suffers from uncertainties in the azimuthal measurements of target wells. Therefore, researchers have proposed several solutions (Gong et al., 2015; Xu et al., 2019; Hirabayashi, 2021; Li et al., 2021) that have shown promise for practical applications. By employing a circumferential array of multiazimuth receivers in the borehole, the borehole azimuthal acoustic reflection imaging method acquires scattered echo signals propagating from the target well. This configuration enables simultaneous detection of the distance and azimuth of the target well. The method achieves three-dimensional (3D) imaging of the target well within tens of meters of the surrounding formation (Qiao et al., 2011; Che et al., 2016; Poedjono et al., 2017; Jervis et al., 2018; Johansen et al., 2019; Ben et al., 2020; Liu et al., 2023; Zhao et al., 2023, 2024a, 2024b). However, the current acoustic detection method requires cable-based logging, which precludes real-time detection of the target well during drilling. It also necessitates halting the drilling process multiple times to re-run the acoustic logging tool, considerably reducing drilling efficiency. Therefore, integrating wireline borehole acoustic reflection imaging with drilling technology is necessary to develop an acoustic-detection-while-drilling method for adjacent well detection, enabling real-time identification of adjacent wells during drilling operations.

Candès et al. (2006) proposed a method for accurately reconstructing original signals from undersampled data. Donoho (2006) introduced the theory of compressed sensing (CS), which garnered widespread attention and found applications across multiple fields (Lustig et al., 2008; Massa et al., 2015; Zhang et al., 2016). CS is a sparse signal–based technique for solving underdetermined linear systems. By employing incoherent sampling at rates far below the Nyquist frequency, it can extract sufficient information from sparse (or compressible) signals to achieve distortion-free reconstruction (Candès, 2008). In acoustic source localization, the actual number of spatial acoustic sources is often sparse relative to the scanned spatial region, satisfying the sparsity requirement of CS theory. CS-based localization methods can achieve estimation accuracy and resolution that are difficult for classical algorithms to achieve and are applicable when the number of acoustic receivers is fewer than the number of acoustic sources (Edelmann and Gaumond, 2011; Simard and Antoni, 2013; Xenaki et al., 2014; Chu et al., 2014).

This study first proposes a new adjacent-well-acoustic-detection-while-drilling method for the real-time detection of target wells, along with an adjacent-well imaging method based on CS. Three-dimensional numerical simulations of the acoustic detection method under drilling conditions are then conducted, and the simulated data are processed using the imaging method. Finally, physical simulation experiments are performed to validate the proposed method, with the experimental data processed through imaging and the inversion results compared against actual parameters to confirm the reliability of the proposed method.

2. Adjacent-well-acoustic-detection-while-drilling method

The adjacent-well-acoustic-detection-while-drilling tool comprises a drill collar, a linear phased array acoustic transmitter, and an acoustic receiver array mounted on the drill collar surface (Fig. 1). The transmitter is positioned in the middle of the tool and comprises Q annular acoustic sources (T_1–T_Q), spaced axially by a distance l, where Q is a positive integer ($Q \geq 2$). The acoustic receiver array includes two identical subarrays, upper and lower, positioned symmetrically above and below the transmitter, respectively. This configuration maintains a short source–receiver distance. Each subarray contains N acoustic receiver stations (R) uniformly distributed along the drill collar axis. Each acoustic receiver station integrates M azimuthal receiving elements (E) distributed circumferentially, with $M \geq 4$. The j-th receiving element of the i-th acoustic receiver station is denoted as R_iE_j ($1 \leq j \leq M$). Receiver station indices are assigned as follows: upper

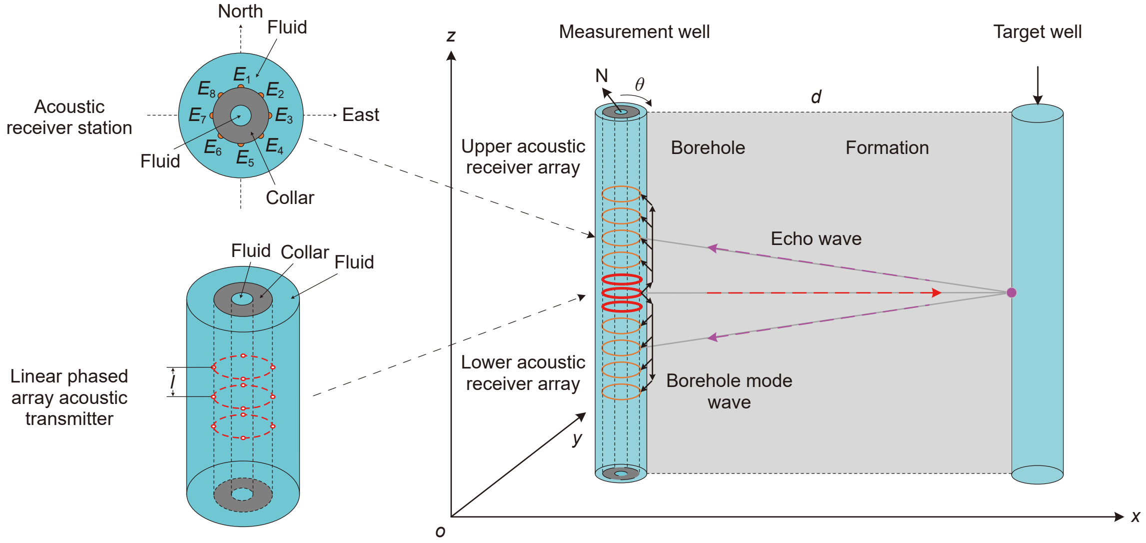

Fig. 1. Schematic of adjacent well acoustic detection while drilling.

array: $1 \le i \le N$; lower array: $-N \le i \le -1$. The cross-sectional view in the top-left corner of Fig. 1 illustrates a representative acoustic receiver station with eight receiving elements (E_1–E_8).

When the logging tool operates, the co-phase and co-amplitude of the transmitter are excited to ensure that the primary acoustic beam radiated from the in-well acoustic source is perpendicularly incident on the borehole wall. The incidence angle of the acoustic wave in the borehole fluid on the borehole wall is approximately 0°, substantially lower than the critical angles for drill collar waves, as well as the first and second critical angles for the formation. These conditions suppress the generation of borehole mode waves—such as drill collar waves, formation-refracted P- and S-waves, and Stoneley waves—while enhancing the P-wave energy radiated by the acoustic transmitter in the borehole fluid into the formation. This energy primarily propagates perpendicular to the borehole axis, which is advantageous for detecting adjacent target wells.

Owing to the short source–receiver distance of the acoustic receiver array, the echo signals from adjacent target wells also propagate approximately perpendicular to the borehole axis—approximately parallel to the plane occupied by the azimuthal receiving elements of the acoustic receiver stations. This configuration shortens the acoustic propagation path and considerably reduces the acoustic attenuation of the echoes, substantially enhancing the P-wave energy of the received signals inside the well. Moreover, accurate determination of the target well's azimuth is assisted by the maximum difference in the echo signals received by the azimuthal receiver elements at any acoustic receiver station.

3. Adjacent-well imaging method based on CS

3.1. CS theory

Let

$$\mathbf{Y} = \boldsymbol{\Psi}\boldsymbol{\Lambda} = \sum_{i=1}^{\eta} \boldsymbol{\Lambda}_i \boldsymbol{\Psi}_i \tag{1}$$

be the linear representation of an $\eta \times 1$ dimensional complex vector of coefficients $\mathbf{Y} = [Y_1, Y_2, \ldots, Y_\eta]^{\mathrm{T}}$ on the basis matrix $\boldsymbol{\Psi} = [\boldsymbol{\Psi}_1, \boldsymbol{\Psi}_2, \ldots, \boldsymbol{\Psi}_\eta]$, where $\boldsymbol{\Lambda} = [\Lambda_1, \Lambda_2, \ldots, \Lambda_\eta]^{\mathrm{T}}$.

If the number of nonzero elements $\|\boldsymbol{\Lambda}\|_0$ in the vector $\boldsymbol{\Lambda}$ satisfies

$$\|\boldsymbol{\Lambda}\|_0 = \xi \ll \eta, \tag{2}$$

then signal $\mathbf{Y}$ is called a sparse signal on the basis matrix $\boldsymbol{\Psi}$. Here, ξ is the sparseness of $\mathbf{Y}$ and $\boldsymbol{\Psi}$ is the sparse basis.

Under the sparse prior condition—where signal $\mathbf{Y}$ possesses sparse coefficients in basis $\boldsymbol{\Psi}$, CS facilitates low-dimensional encoding through linear projection. The high-dimensional signal may therefore be accurately recovered from its compressed low-dimensional counterpart, as demonstrated in foundational work by Donoho (2006). In general, a linear transformation on signal $\mathbf{Y}$

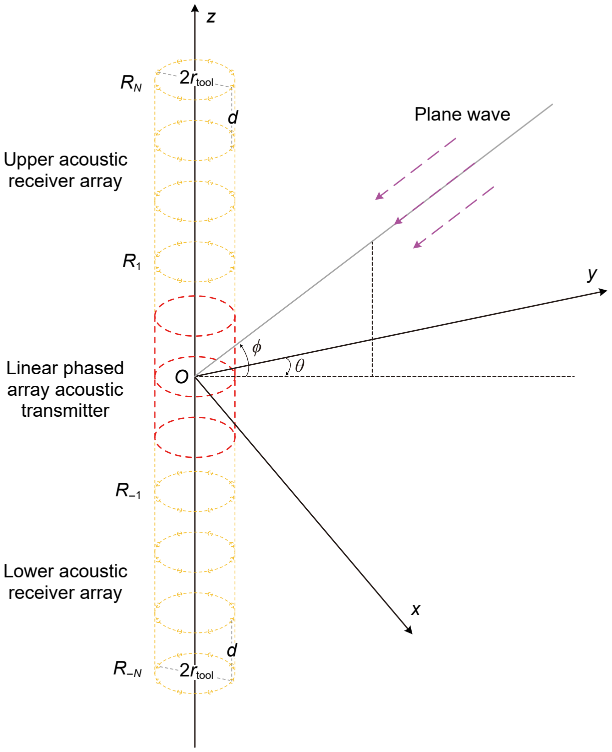

Fig. 2. Schematic of the acoustic receiver array and incident plane wave.

using an $\mu \times \eta$ dimensional observation matrix $\mathbf{\Phi}$ yields a $\mu \times 1$ dimensional observation vector as follows:

$$\mathbf{X} = \mathbf{\Phi}\mathbf{Y} = \mathbf{\Phi}\mathbf{\Psi}\mathbf{\Lambda} = \mathbf{\Theta}\mathbf{\Lambda}, \tag{3}$$

where $\mathbf{X} = [X_1, X_2, ..., X_\mu]^{\mathrm{T}}$ is the observation vector and $\mathbf{\Theta} = \mathbf{\Phi}\mathbf{\Psi}$ is the CS matrix.

High-probability signal reconstruction is achievable under the restricted isometry property of sensing matrix $\mathbf{\Theta}$ (Candes et al., 2006; Candes, 2008). This property is probabilistically guaranteed when a random measurement matrix $\mathbf{\Phi}$ complies with requirement $\mu \geq C\xi \log(\eta/\xi)$, wherein constant C dictates reconstruction fidelity. Presuming that signal $\mathbf{Y}$ is sparse, the underdetermined system of equations $\mathbf{X} = \mathbf{\Theta}\mathbf{\Lambda}$ can be solved by minimizing the L_0 norm:

$$\begin{aligned} &\widehat{\mathbf{\Lambda}} = \mathrm{argmin}\|\mathbf{\Lambda}\|_0 \\ &\text{s.t. } \mathbf{X} = \mathbf{\Theta}\mathbf{\Lambda} \end{aligned}. \tag{4}$$

Under certain conditions, the L_p norm $(0 < p \leq 1)$ approximates the L_0 norm, thereby imposing a sparsity constraint on $\mathbf{\Lambda}$ and achieving good $\mathbf{\Lambda}$ reconstruction. Signal reconstruction is a core problem in CS theory. Existing reconstruction algorithms include orthogonal matching pursuit (OMP), the basis pursuit algorithm, and others (Tropp and Gilbert, 2007; Huggins and Zucker, 2007; Needell and Vershynin, 2010).

3.2. *Mathematical model of echo signals for adjacent-well acoustic detection during drilling*

Under far-field criteria, which require the radial distance of the target well from the measurement well axis to be much greater than the wavelength and receiver array scale, echoes from the target well are treatable as plane waves (Bennett, 2019; Zhao et al., 2025). With the acoustic array midpoint set as the coordinate origin (O in Fig. 2), the unit direction vector $\mathbf{v}$ for planar echo propagation satisfies

$$\mathbf{v}(\theta, \phi) = -(\cos\phi\sin\theta, \cos\phi\cos\theta, \sin\phi)^{\mathrm{T}}. \tag{5}$$

The transposition operation is represented by $(.)^{\mathrm{T}}$ in this formula, with θ and ϕ indicating the plane wave's azimuthal and vertical angles, respectively. Here, the azimuth is measured clockwise starting from North (i.e., the y-axis positive direction, set at 0°) and $-90^\circ \leq \phi \leq 90^\circ$.

The coordinate vector of the receiving element in the acoustic receiver array is given by

$$\begin{aligned} &\mathbf{x}_{i,j}^{\mathrm{R}} = \left(x_{i,j}, y_{i,j}, z_{i,j}\right)^{\mathrm{T}} \\ &= \begin{cases} [r_{\mathrm{tool}}\sin[(j-1)\varepsilon], r_{\mathrm{tool}}\cos[(j-1)\varepsilon], -\mathrm{TRSP} + (i+1)d]^{\mathrm{T}}, & i = -N, ..., -1, \\ [r_{\mathrm{tool}}\sin[(j-1)\varepsilon], r_{\mathrm{tool}}\cos[(j-1)\varepsilon], \mathrm{TRSP} + (i-1)d]^{\mathrm{T}}, & i = 1, ..., N, \quad j = 1, ..., M, \end{cases} \end{aligned} \tag{6}$$

where $\mathbf{x}_{i,j}^{\mathrm{R}}$ represents the coordinate vector of receiving element j on acoustic receiver station i and ε represents the angular interval of the adjacent receiving elements. Additionally, r_{tool} is the radius of the acoustic receiver station, d is the spacing between adjacent acoustic receiver stations, and TRSP is the minimum source distance for the acoustic receiver stations.

Given the presence of K target wells adjacent to the measurement well, the relative time delay $\sigma_{i,j,k}$ of the k-th echo at the receiving element R_iE_j with respect to origin O is formulated as follows:

$$\begin{aligned} &\sigma_{i,j,k} = \frac{\mathbf{v}_k^T\mathbf{x}_{i,j}^R}{c} \\ &= \begin{cases} \dfrac{-\{r_{\mathrm{tool}}\cos\phi_k\cos[\theta_k - (j-1)\varepsilon] + [-\mathrm{TRSP} + (i+1)d]\sin\phi_k\}, \quad i = -N, ..., -1,}{c} \\ \dfrac{-\{r_{\mathrm{tool}}\cos\phi_k\cos[\theta_k - (j-1)\varepsilon] + [\mathrm{TRSP} + (i-1)d]\sin\phi_k\}, \quad i = 1, ..., N,}{c} \end{cases} \\ &j = 1, ..., M, \quad k = 1, ..., K, \end{aligned} \tag{7}$$

where c is the echo propagation velocity.

Assume that signal waveform $s_k(t)$ received at reference point O corresponds to echo k from the target well. Further assume that each receiving element in the array receives stationary Gaussian white noise with the same bandwidth as the echo signal and with no correlation to the echo signal. After a propagation delay, the waveform $p_{i,j}(t)$ received by R_iE_j is the superposition of all echo signals from the target well:

$$p_{i,j}(t) = \sum_{k=1}^{K} s_k\left(t - \sigma_{i,j,k}\right) + n_{i,j}(t), \tag{8}$$

where $n_{i,j}(t)$ is the noise waveform received by receiving unit R_iE_j.

A Fourier transform on Eq. (8) converts the delay in the time domain to a phase shift in the frequency domain. On discretized data, the phase shift is obtained at each frequency point:

$$P_{i,j}(f_l)=\sum_{k=1}^{K}a_{i,j,k}(f_l,c,\theta_k,\phi_k)S_k(f_l)+N_{i,j}(f_l),\qquad l=1,\ldots,L. \tag{9}$$

Eq. (9) is expressed in vector form as follows:

$$\mathbf{P}(f_l)=\mathbf{A}(f_l,c,\theta,\phi)\mathbf{S}(f_l)+\mathbf{N}(f_l),\qquad l=1,\ldots,L, \tag{10}$$

where f_l represents the l-th frequency point within the operating frequency band and L represents the number of discrete frequency points. The terms $\mathbf{P}(f_l)$, $\mathbf{S}(f_l)$, $\mathbf{N}(f_l)$, and $\mathbf{A}(f_l,c,\theta,\phi)$ denoting the received array data, signal vector, noise vector, and phase-shift matrix in the frequency domain, respectively, are respectively computed as follows:

$$\begin{aligned}
&\mathbf{P}(f_l)=\left[P_{-N,M}(f_l),\ldots,P_{-1,2}(f_l),P_{-1,1}\left(f_j\right),P_{1,1}\left(f_j\right),P_{1,2}(f_l),\ldots,P_{i,j}(f_l),\ldots,P_{N,M}(f_l)\right]^{\mathrm{T}}\\
&\mathbf{S}(f_l)=[S_1(f_l),S_2(f_l),\ldots,S_k(f_l),\ldots,S_K(f_l)]^{\mathrm{T}}\\
&\mathbf{N}(f_l)=\left[N_{-N,M}(f_l),\ldots,N_{-1,2}(f_l),N_{-1,1}\left(f_j\right),N_{1,1}(f_l),N_{1,2}(f_l),\ldots,N_{i,j}(f_l),\ldots,N_{N,M}(f_l)\right]^{\mathrm{T}},\\
&\mathbf{A}(f_l,c,\theta,\phi)=\begin{bmatrix}\mathbf{a}(f_l,c,\theta_1,\phi_1),\mathbf{a}(f_l,c,\theta_2,\phi_2),\ldots,\\ \mathbf{a}(f_l,c,\theta_k,\phi_k),\ldots,\mathbf{a}(f_l,c,\theta_K,\phi_K)\end{bmatrix}
\end{aligned} \tag{11}$$

where $\mathbf{a}(f_l,c,\theta_k,\phi_k)$ denotes a phase-shift vector in the frequency domain and

$$\begin{aligned}
\mathbf{a}(f_l,c,\theta_k,\phi_k)&=\begin{bmatrix}a_{-N,M}(f_l,c,\theta_k,\phi_k),\ldots,\\ a_{-1,2}(f_l,c,\theta_k,\phi_k),a_{-1,1}(f_l,c,\theta_k,\phi_k),\\ a_{1,1}(f_l,c,\theta_k,\phi_k),a_{1,2}(f_l,c,\theta_k,\phi_k),\ldots,\\ a_{i,j}(f_l,c,\theta_k,\phi_k),\ldots,a_{N,M}(f_l,c,\theta_k,\phi_k)\end{bmatrix}^{\mathrm{T}}\\
&=\begin{bmatrix}\exp\left(-j2\pi f_l\sigma_{-N,M,k}\right),\ldots,\\ \exp\left(-j2\pi f_l\sigma_{-1,2,k}\right),\exp\left(-j2\pi f_l\sigma_{-1,1,k}\right),\\ \exp\left(-j2\pi f_l\sigma_{1,1,k}\right),\exp\left(-j2\pi f_l\sigma_{1,2,k}\right),\ldots,\\ \exp\left(-j2\pi f_l\sigma_{i,j,k}\right),\ldots,\exp\left(-j2\pi f_l\sigma_{N,M,k}\right)\end{bmatrix}^{\mathrm{T}}.
\end{aligned} \tag{12}$$

3.3. CS-based adjacent-well imaging method

After discretizing the spatial location of the near-well formation, we obtain a set of discretized spatial location nodes $\{(\theta_1,\phi_1),(\theta_2,\phi_2),\ldots,(\theta_I,\phi_I)\}$. The number of spatial location nodes I far exceeds the number of target wells K around the well. In the frequency domain, the redundant phase-shift matrix $\mathbf{G}$ corresponding to the discretized spatial location nodes is given by

$$\mathbf{G}(f_l,c,\theta,\phi)=\begin{bmatrix}\mathbf{a}(f_l,c,\theta_1,\phi_1),\mathbf{a}(f_l,c,\theta_2,\phi_2),\ldots,\\ \mathbf{a}(f_l,c,\theta_K,\phi_K),\ldots,\mathbf{a}(f_l,c,\theta_I,\phi_I)\end{bmatrix} \tag{13}$$

and the signal vector $\tilde{\mathbf{S}}$ corresponding to $\mathbf{G}$ is given by

$$\tilde{\mathbf{S}}(f_l)=[S_1(f_l),S_2(f_l),\ldots,S_K(f_l),\ldots,S_I(f_l)]^{\mathrm{T}}. \tag{14}$$

Eq. (10) can be expanded as follows:

$$\mathbf{P}(f_l)=\mathbf{G}(f_l,c,\theta,\phi)\tilde{\mathbf{S}}(f_l)+\mathbf{N}(f_l),\qquad l=1,\ldots,L. \tag{15}$$

As the number of adjacent target wells is sufficiently smaller than the number of spatial nodes I, the frequency-domain signal vector $\tilde{\mathbf{S}}$ is sparse over the discretized spatial node set. The nonzero elements in $\tilde{\mathbf{S}}$ share a one-to-one correspondence with the spatial positions of the adjacent target wells. In particular, when a single adjacent target well exists, $\tilde{\mathbf{S}}$ contains exactly one nonzero element. Treating $\mathbf{G}$ as the CS measurement matrix $\boldsymbol{\Theta}$ in Eq. (3), $\tilde{\mathbf{S}}$ can be fully recovered with high probability under CS theory. The spatial locations of the adjacent target wells can then be estimated by identifying the positions of the nonzero values in $\tilde{\mathbf{S}}$, i.e.,

$$\begin{aligned}&\tilde{\mathbf{S}}=\operatorname{argmin}\|\tilde{\mathbf{S}}\|_0\\ &\text{s.t. }\mathbf{P}=\mathbf{G}\tilde{\mathbf{S}}+\mathbf{N}\end{aligned}. \tag{16}$$

In practical scenarios, owing to contamination from the frequency-domain noise vector $\mathbf{N}$, the number of nonzero elements in the reconstructed signal vector $\tilde{\mathbf{S}}$ exceeds the number of adjacent target wells. These spurious nonzero components occupy spatial positions not occupied by target wells. To enhance the positioning accuracy, this research synthesizes information across multiple frequencies within the operational bandwidth. The frequency-domain signal vectors $\tilde{\mathbf{S}}$ at discrete frequency points are reconstructed through stacking and averaging to obtain

$$\tilde{\mathbf{S}}_L=\frac{1}{L}\sum_{l=1}^{L}\tilde{\mathbf{S}}(f_l). \tag{17}$$

This study employs OMP, which is less computationally complex than other signal reconstruction algorithms. After iteratively identifying the position of maximum correlation between the measurement matrix and compressed sampled signal, OMP solves the least-squares problem to approximate the signal solution (Tropp and Gilbert, 2007). This process is repeated until the iteration count is strictly less than the sparsity level, ultimately outputting the index set of maximally correlated atoms and the reconstructed signal.

4. Numerical simulation and imaging processing

4.1. Numerical simulation of an acoustic field with no target wells

4.1.1. Infinite fluid medium containing an adjacent-well-acoustic-detection-while-drilling tool

As proposed in Section 2, the adjacent-well detection method based on the acoustic phased array was simulated during drilling using the 3D Cartesian coordinate finite-difference method. First, a 3D acoustic field computational model was constructed in an infinite fluid medium with no measurement wells or adjacent target wells. An adjacent-well-acoustic-detection-while-drilling tool was placed in the medium. The linear phased array acoustic transmitter comprised three annular sources (T_1–T_3), with an axial spacing of 0.05 m, operating at a central frequency of 15 kHz. The material properties of the drill collars and fluid used in the numerical simulations are listed in Table 1.

Wavefield snapshots at different time steps (Fig. 3) show the propagation of drill collar waves and fluid P-waves within the wavefield. The drill collar waves propagated considerably faster than the fluid P-waves. Identical time delays and amplitudes were applied to the excitation signals of each array element in the acoustic source, maximizing the radiation capability in the horizontal direction. The primary acoustic beam was distributed symmetrically above and below the source, with the acoustic field exhibiting axial symmetry about the tool's central axis.

4.1.2. Fluid-filled borehole containing the adjacent-well-acoustic-detection-while-drilling tool

A fluid-filled measurement borehole without adjacent target wells was considered for subsequent analysis. The adjacent-well-

Table 1
Parameters of numerical calculation.

		P-wave velocity, m/s	S-wave velocity, m/s	Density, kg/m^3	Radius, m
Fluid		1500	0	1000	0.045
Drill collar		5860	3130	7800	0.1016
Formation	Sandstone	3810	2380	2480	Not applicable
	Mudstone	2540	1300	2000	
	Limestone	6096	3350	2690	

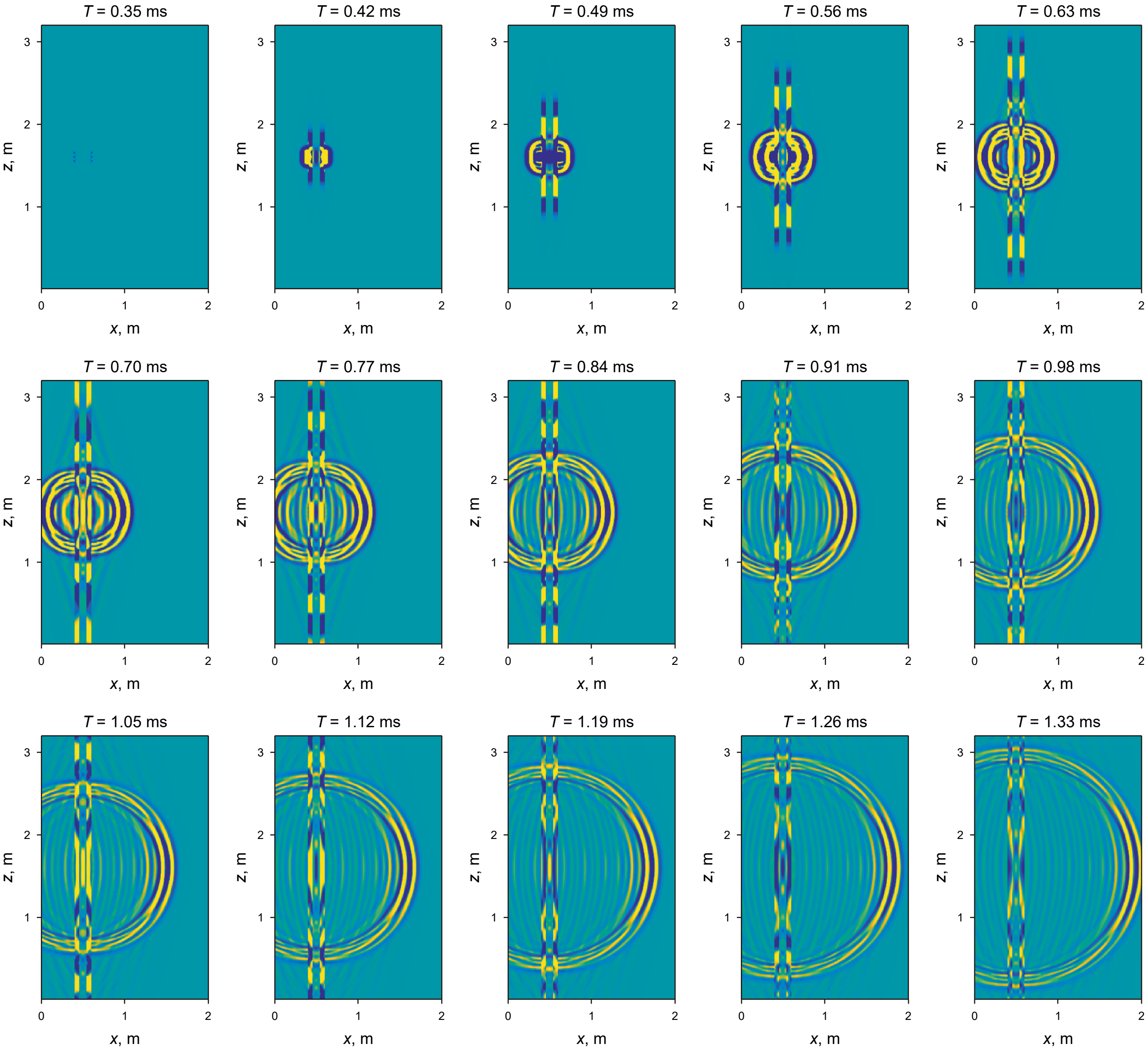

Fig. 3. Wavefield snapshots at different time steps (*T*).

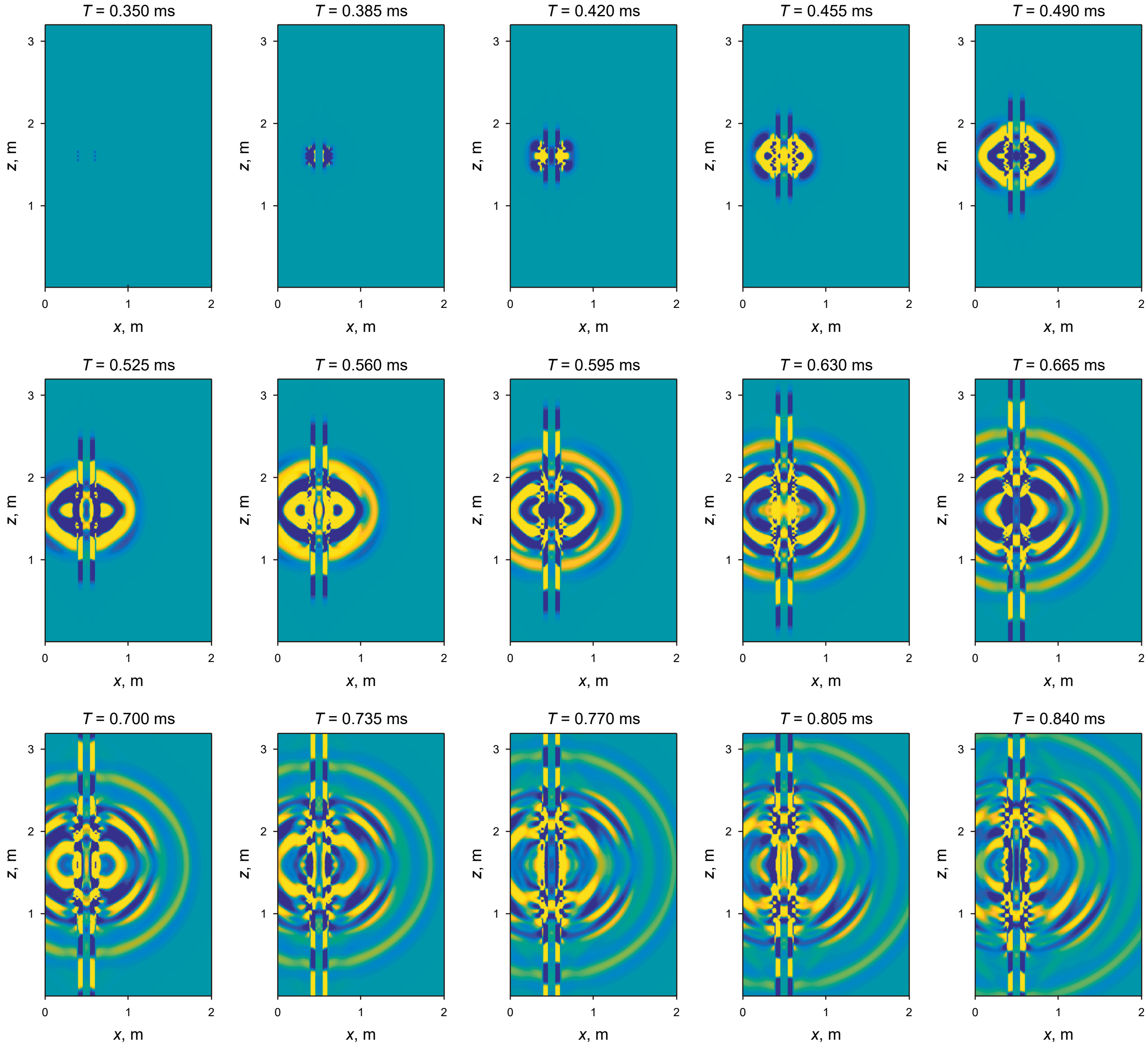

Fig. 4. Wavefield snapshots in the sandstone formation at different time steps (*T*).

acoustic-detection-while-drilling tool was immersed in this borehole, and a 3D acoustic field computational model was developed under drilling conditions. The parameters of the linear phased array source were the same as those mentioned in Section 4.1.1. The formation types adjacent to the measurement borehole were sandstone, mudstone, and limestone. The acoustic and physical parameters of the drill collar, fluid, and formations used in the numerical simulation are listed in Table 1. Fig. 4 presents wavefield snapshots in a sandstone formation at different time steps. Identical time delays and amplitudes were applied to the excitation signals of each array element in the acoustic source, which resulted in an acoustic field symmetric about the tool's central axis. The acoustic source generated P- and S-waves in the formation near the borehole. In the vertical plane, the radiation beams of both wave types were symmetrically distributed above and below the source. The P-wave exhibits its maximum radiation amplitude in the horizontal direction, whereas the S-wave radiation in the same direction is nearly negligible. This result suggests that P-waves are more effective for detecting adjacent wells that parallel or subparallel to the measurement well, whereas S-waves are better suited for detecting adjacent wells that intersect the measurement well at a large angle. Compared with the wavefield pattern shown in Fig. 3, the wavefield in Fig. 4—obtained when the drill collar is placed in a fluid-filled borehole—contains additional borehole mode waves (such as drill collar waves, refracted P- and S-waves, and Stoneley waves) and body waves (e.g., P- and S-waves) radiating into the formation. The presence of the borehole increases the variety of mode-wave types, resulting in a more

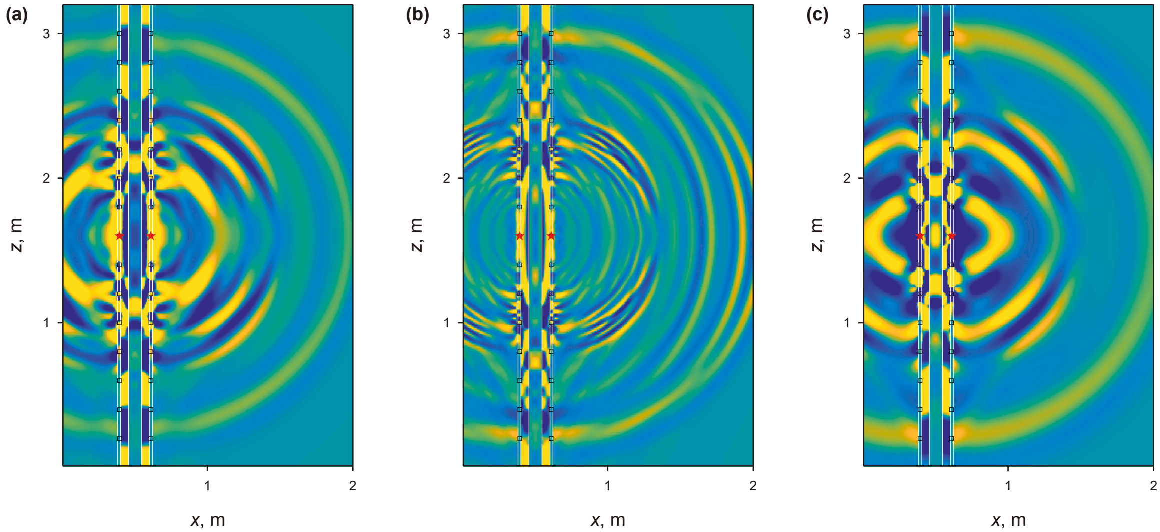

Fig. 5. Comparison of wavefield snapshots in the **(a)** sandstone, **(b)** mudstone, and **(c)** limestone formations. Red pentagrams and black rectangles denote the acoustic source and receiver position, respectively, and the white solid lines indicate the boundary between the drill collar and borehole.

complex acoustic field than that produced when the drill collar is placed in an infinite fluid domain.

Fig. 5 shows wavefield snapshots in different formation types for comparison. As observed, when the near-borehole formation comprises sandstone, mudstone, or limestone, the P- and S-waves generated by the acoustic source display similar energy distribution characteristics. Therefore, only the sandstone formation is considered in subsequent analyses.

4.2. *Numerical simulation and imaging of acoustic fields with adjacent target wells*

4.2.1. *Scattered wavefield resulting from an adjacent target well near the measurement borehole*

An adjacent-well-acoustic-detection-while-drilling tool was deployed in a measurement well in a scenario involving a borehole and an adjacent target well (Fig. 1). The formation adjacent to the borehole comprised sandstone, with the target well oriented vertically. Its position was defined by an azimuthal angle (θ) of 112.5° relative to the measurement well and a radial separation (d) of 5.0 m. The target well was fluid-filled, and both the measurement and target wells had identical borehole diameters ($d_1 = d_2 = 0.24$ m). The upper and lower acoustic receiver arrays were structurally identical and symmetrically positioned on either side of the linear phased array acoustic transmitter. Each array comprised seven acoustic receiver stations (R) uniformly spaced along the drill collar axis, with a minimum source-to-receiver distance of 0.2 m and an axial spacing of 0.2 m. An additional receiver station, R_0, was placed at the center of the linear phased array transmitter. At every receiver station ($r = 0.108$ m), the drill collar contained eight uniformly spaced azimuthal elements (E) along its circumference. In addition to all eight elements per station, an receiver element, E_v, was positioned at $\theta = 112.5°$, azimuthally aligned with the target well.

Fig. 6 presents 3D wavefield snapshots of the full wavefield—including direct and scattered waves—at different time steps. The linear phased array source generated P- and S-waves within the formation. When these waves encountered the target well, they produced backscattered echoes containing multiple wave modes, including scattered PP-waves, mode-converted PS-waves, mode-converted SP-waves, and scattered SS-waves. Fig. 7 displays the variable-density plots of echo waveforms recorded at all acoustic receiver stations. Fig. 8(a) shows the echo waveforms at different source-to-receiver distances, with receiver elements sequentially numbered from $R_{-7}E_v$ to R_7E_v. The receiver element E_v, azimuthally aligned with the target well, was optimally positioned to receive the strongest echoes. Fig. 8(b) plots echo amplitudes versus source-to-receiver distance for different wave modes. The PP-waves exhibited the highest amplitude, followed by PS and SP converted waves, whereas SS-waves had the lowest amplitude. The amplitude decreased in the order of PP-waves > PS/SP converted waves > SS-waves. The PP-wave amplitude gradually decreased with increasing source-to-receiver distance.

Fig. 9(a) shows the echo waveforms recorded at different azimuths by receiver station R_2, with elements sequentially numbered from R_2E_1 to R_2E_8. The arrival times of the echoes showed an approximately sinusoidal variation with azimuth. Elements E_3 and E_4, located closest to the azimuth of the target well, recorded the earliest arrival times and strongest echo amplitudes. Fig. 9(b) plots the echo amplitudes of different wave modes versus azimuthal angle, with all wave modes showing peak amplitudes at 112.5°, coinciding precisely with the azimuth of the target well.

The formation space around the well was discretized into an azimuthal-angle imaging range of 0°–360° at 0.5° intervals and a vertical-angle imaging range of −90°–90° at 1° intervals. As the number of spatial position nodes far exceeded the number of target wells, the frequency-domain signal vector of the target well was sparse. Azimuth imaging of the target well was performed using the 3D slowness time coherence (3D-STC) method (Bennett, 2019) and the CS method (Fig. 10(a) and (b), respectively). In Fig. 10(a), the target well appears as a high-intensity imaging zone. The azimuth and vertical angles corresponding to the maximum point (black asterisk) within this zone are 116° and 0°, respectively, deviating from the true azimuth of the target

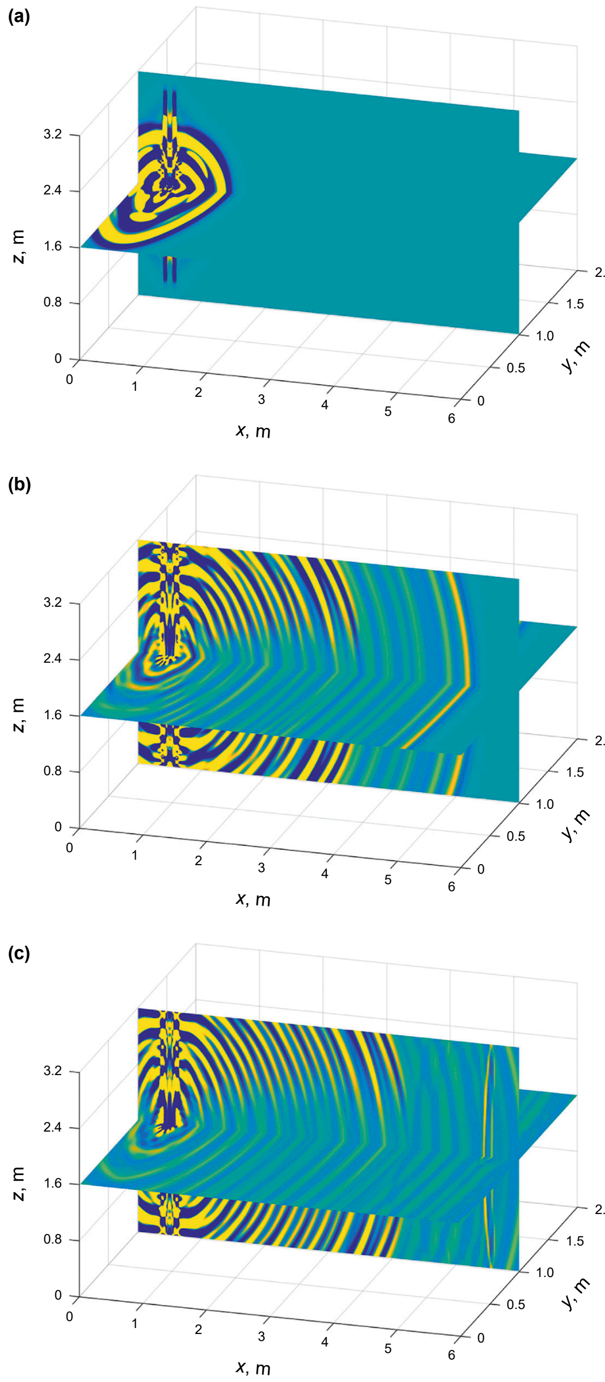

Fig. 6. 3D wavefield snapshots of the full waves (direct and scattered waves) at different time steps: $T =$ **(a)** 0.63, **(b)** 1.65, and **(c)** 1.96 ms.

well by 3.5°. In Fig. 10(b), the target well is represented as a maximum-intensity point at (112.5°, 0°) in the azimuthal imaging diagram, perfectly matching the true azimuth of the target well.

After extracting the imaging maxima corresponding to the vertical-angle positions from Fig. 10(a) and (b), the imaging values were obtained at different azimuths. The normalized azimuth positioning curve of the target well is displayed in Fig. 10(c). Compared to the relation curve between PP echo amplitude and azimuth in Fig. 9(b) and the normalized azimuth positioning curve obtained using the 3D-STC method, the normalized azimuth positioning curve obtained used the CS method is sharper. This indicates that the CS-based adjacent-well imaging method provides higher azimuth resolution than the echo amplitude and 3D-STC methods.

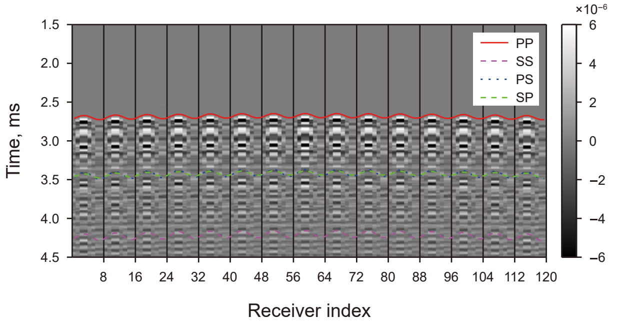

Fig. 7. Variable-density displays of the echo waveforms from all acoustic receiver stations. The receiver elements are numbered in order of their azimuthal positions E followed by their source-to-receiver distances R: $R_{-7}E_1$–$R_{-7}E_8$, …, $R_{-1}E_1$–$R_{-1}E_8$, R_0E_1–R_0E_8, R_1E_1–R_1E_8, …, R_7E_1–R_7E_8.

4.2.2. Radial distance adjustment of the target well

We varied the target well's radial distance d (1.0, 2.0, 5.0, 10.0, and 15.0 m) and captured variable-density echo waveforms (Fig. 11). At $d = 15.0$ m, the PP echo displayed considerable signal retardation, converging toward a plane-wave morphology. Single-shot echoes at this distance generated a 3D spatial scanning image (Fig. 12), with the imaging profile referenced to the target well's scattered-wave sagittal plane. Crucially, for radially distant and parallel well configurations, PP-wave echoes provided superior scanning images; meanwhile, other wave modes (PS, SP, or SS) resulted in markedly lower quality. This difference was correlated with the relative amplitudes of the different scattering modes. Fig. 13 plots the amplitude of the PP-wave echoes versus radial distance from the target well at receiver element R_2E_v. With increasing radial distance, the PP-wave amplitude gradually decreased at a progressively diminishing decay rate.

Figs. 14 and 15 present the azimuthal imaging results after applying the CS method to the single-shot PP echo waveforms at $d = 1.0$ and 15.0 m, respectively. In both the near and far fields of the measurement well, the target well appeared as a local maximum in the azimuthal imaging diagram. The coordinates of this maximum are (112.5°, 0°), again consistent with the azimuthal and inclination angles of the target well.

4.2.3. Diameter adjustment of the target well

The diameter of the target well was varied as 1.0, 1.2, 1.4, and 1.6 times the initial diameter (0.24 m), as shown in Fig. 16. Fig. 17(a) displays the echo waveforms at different source–receiver distances, where the receiver elements are sequentially numbered from R_1E_v to R_7E_v. Increasing the diameter of the target well shortened the arrival time and enhanced the amplitude of the PP echo. This trend occurred because within the first Fresnel zone radius, the shortest ray path extends first from the acoustic source to the reflection point on the reflective-surface interface and then

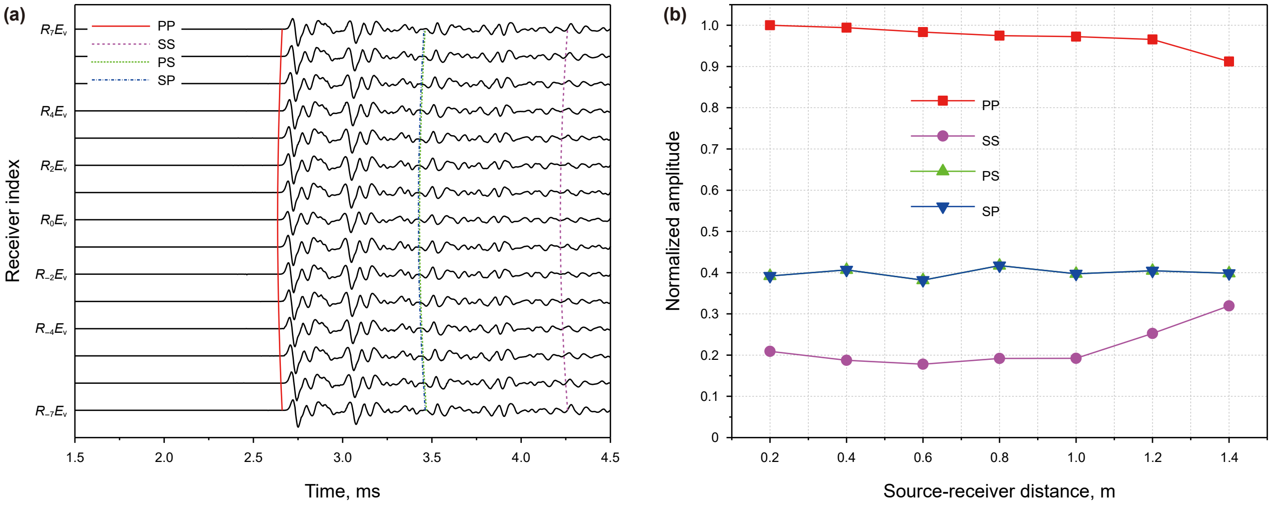

Fig. 8. (**a**) Echo waveforms at different source-to-receiver distances; (**b**) echo amplitudes versus source-to-receiver distance in different wave modes.

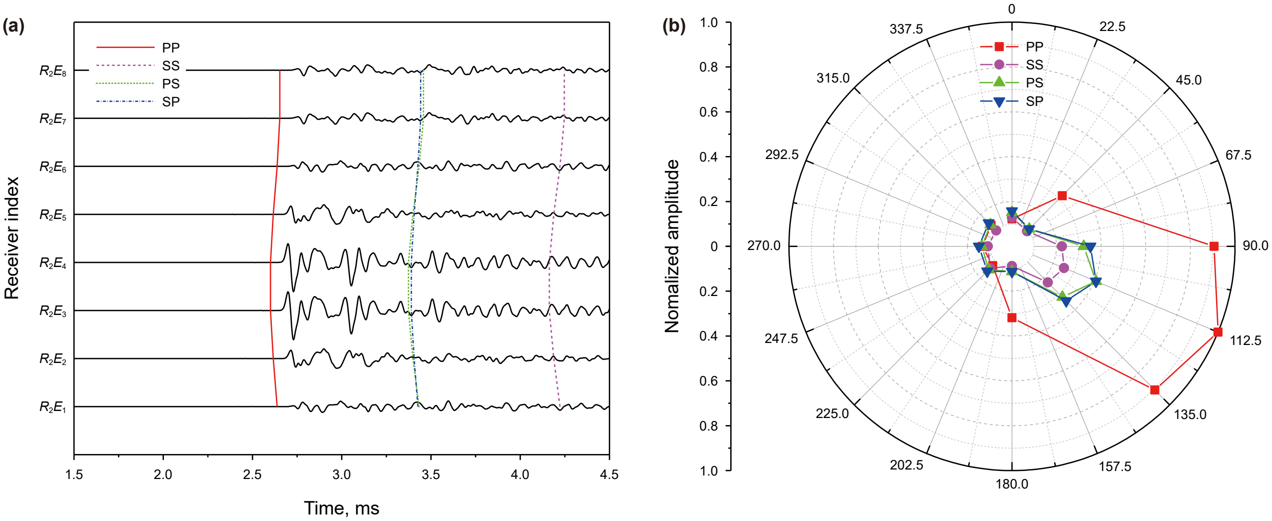

Fig. 9. (**a**) Echo waveforms at different azimuths R_2 at the receiver station; (**b**) echo amplitude versus azimuth in different wave modes.

to the receiver. Comparing this reflection path with the ray paths of other points on the interface, the radius of the first Fresnel zone is the distance between two points on the interface where the path difference equals one-half the wavelength ($\lambda/2$) (Qian, 2010). A larger well diameter increases the number of scattering points that generate scattered waves, enhancing the constructive interference and hence the PP echo amplitude. In addition, when the well axis is fixed, increasing the diameter reduces the propagation distance of the acoustic field (which is radiated from the acoustic source within the well and scattered by the target well) to the downhole receiver, shortening the arrival time of the PP echo. Fig. 17(b) plots the PP echo amplitudes as functions of source–receiver distance for different diameters of the target well. The amplitude increased with increasing well diameter but decreased with increasing source–receiver distance.

Fig. 18(a) displays the echo waveforms at different azimuths at the R_2 receiver station. Here, the receiving elements are sequentially numbered from R_2E_1 to R_2E_8. For all diameters of the target well, the arrival time of the PP echo varied approximately sinusoidally with azimuth. The receiving elements closest to the target well's azimuth (E_3 and E_4) consistently recorded the strongest echoes at the earliest arrival times. Fig. 18(b) illustrates the azimuthal variation of the PP echoes. Regardless of target well diameter, the amplitude of the PP echoes was maximized at 112.5°, matching the actual azimuth of the target well. Fig. 19 plots the normalized PP echo amplitude versus target well diameter at receiving element R_2E_v. The relation is almost linear.

Fig. 20 displays the azimuthal image and normalized azimuthal positioning curve of the PP echo from an adjacent

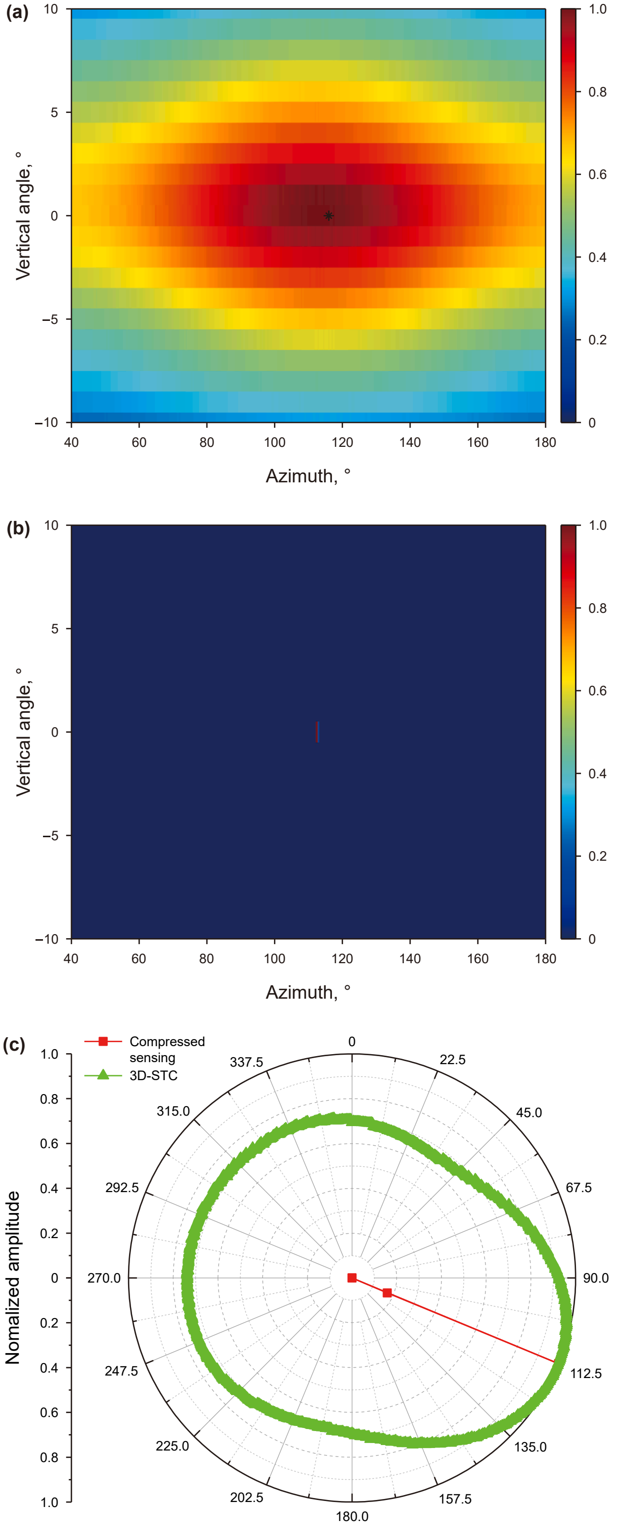

Fig. 10. Azimuthal imaging based on **(a)** 3D-STC and **(b)** CS; **(c)** normalized azimuthal positioning curves of scattered PP-waves from an adjacent target well.

target well with a diameter of 0.384 m (1.6 times the initial diameter). Enlarging the target well diameter enhanced the amplitude of the PP echo originating from the target well. Consequently, the imaging quality of the target well is substantially higher in Fig. 20 than in Fig. 10.

4.2.4. Adjustment of relative angle between the target and measurement wells

To rotate the target well axis within the x–z plane, the angle α_{x-z} between the target and measurement wells was varied as 0°, 10°, 20°, 30°, and 40° (Fig. 21). The target well exhibited a diameter of 0.24 m. Temporal snapshots of the echo wavefield are presented in Fig. 22, revealing multimodal wave components (PP, SS, PS, and SP) originating from the target well. Variation in the angle α_{x-z} shifted the dominant energy propagation direction of these modes, concurrently amplifying SS-wave energy within a depth (z) interval of 0.0–3.0 m.

Fig. 23 displays the echo waveforms as α_{x-z} was varied from 0° to 40°. The first column shows the waveforms at varying source–receiver distances, where the receiving elements are sequentially numbered from $R_{-7}E_{\mathrm{V}}$ to R_7E_{V}. The second column presents the waveforms arriving at the R_2 acoustic receiver station from different azimuthal angles, where the elements are ordered from R_2E_1 to R_2E_8. Regardless of α_{x-z}, the arrival times and azimuths of each echo mode sinusoidally varied over time. The echoes from elements E_3 and E_4 (closest to the target well) consistently exhibited the earliest arrivals and highest amplitudes.

Fig. 24(a) shows the echo waveforms at the receiving element R_2E_{V}. Increasing α_{x-z} progressively shortened the arrival times of the different mode echoes, reflecting the shortening propagation paths of the incident and scattered waves. Increasing α_{x-z} did not clearly affect the amplitudes of the PP echoes and converted waves but gradually increased the amplitude of the SS echoes. When the amplitudes of the echo modes were plotted as functions of α_{x-z} (Fig. 24(b)), the amplitude of the PP echo was found to slightly decrease with increasing α_{x-z}, whereas the converted wave remained largely unchanged and the amplitude of the SS echo markedly increased. The PP echo was stronger than the SS echo at $\alpha_{x-z} < 20°$, of comparable amplitude to the SS echoes at $\alpha_{x-z} = 20°$, and weaker than the SS echo at $\alpha_{x-z} > 20°$. Therefore, when the target well near the borehole is approximately parallel to the measurement well (i.e., the relative angle is small), the PP echoes provide the optimal detection result. Conversely, the SS echoes yield superior detection results at large relative angles.

Panels (a) and (b) of Fig. 25 show the azimuthal imaging results of adjacent target wells near the measurement well at $\alpha_{x-z} = 10°$ and 20°, respectively, derived from the PP echoes. Panels (c) and (d) display the corresponding results for 30° and 40°, respectively, derived from the SS echoes. The CS-based adjacent-well imaging method achieves considerably high spatial imaging resolution. Besides pinpointing the azimuth of the target well, it estimates the relative angle between the target and measurement wells.

5. Physical simulation and imaging processing

5.1. Experimental model

The physical simulation experiment employed an adjacent-well-acoustic-detection-while-drilling tool with three annular sources operating at a dominant frequency of approximately 15 kHz. The receiver array comprised eight acoustic receiver stations: four stations (R_1–R_4) positioned above the source and four stations (R_{-1}–R_{-4}) positioned below it. We set the source-to-receiver distance to 0.8 m, with a separation distance of

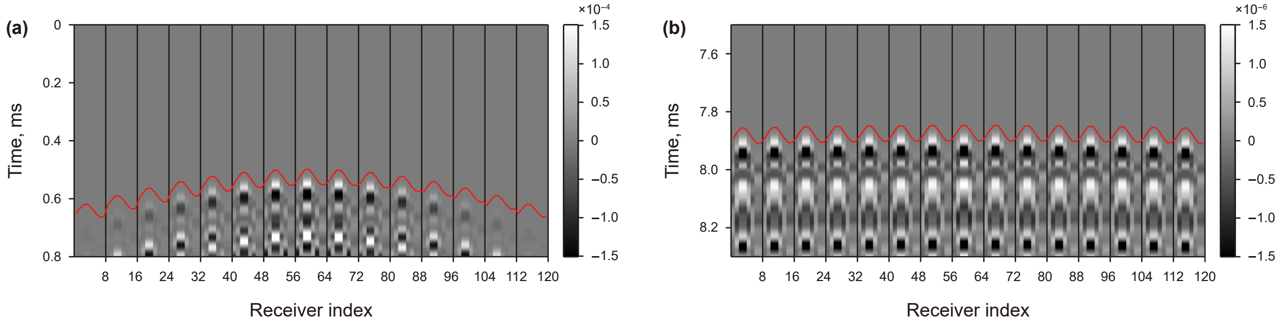

Fig. 11. Variable-density displays of the echo waveforms at all receiver stations at **(a)** $d = 1.0$ m, **(b)** $d = 15.0$ m. The receiver elements are numbered in order of their azimuthal angle E followed by their source-to-receiver distance R: $R_{-7}E_1$–$R_{-7}E_8$, …, $R_{-1}E_1$–$R_{-1}E_8$, R_0E_1–R_0E_8, R_1E_1–R_1E_8, …, R_7E_1–R_7E_8. The red line indicates the theoretical travel-time curve of the PP echoes.

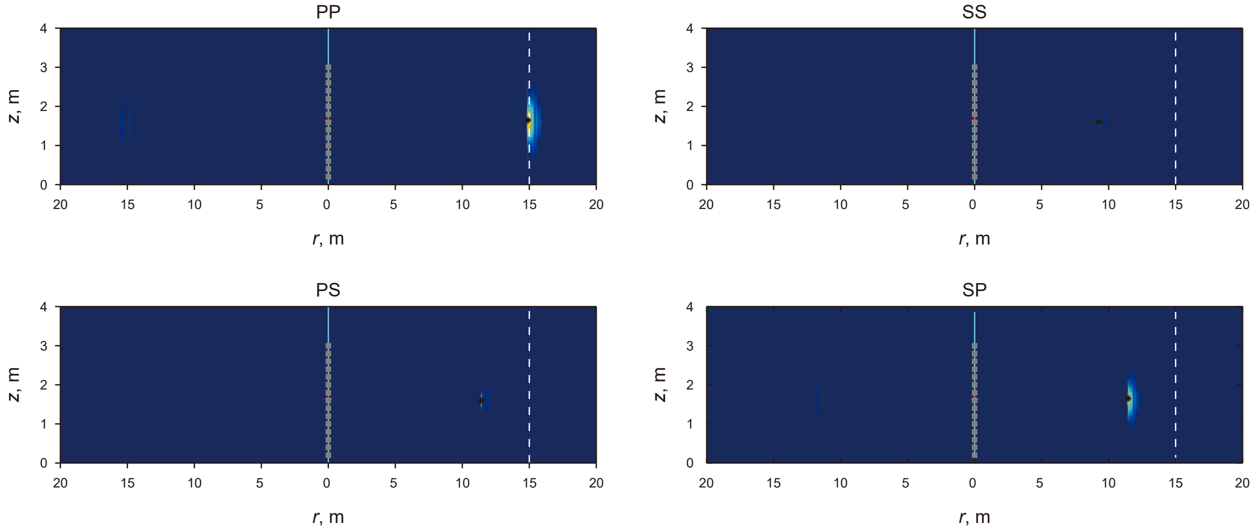

Fig. 12. 3D spatial scanning image of the target well at $d = 15.0$ m. The white dashed lines indicate the target well axis, and the black asterisk represents the local maximum imaging point, which is closest to the well axis.

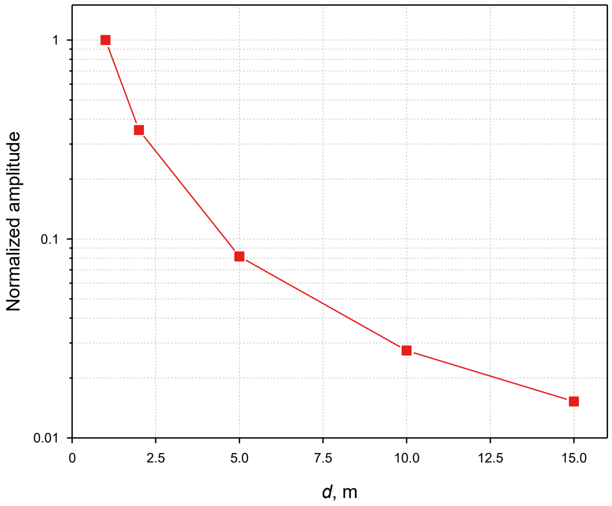

Fig. 13. Relation between PP-wave echo amplitude and radial distance from the target well for receiver element R_2E_v.

0.2 m between adjacent stations. Each receiver station comprised a circumferential array of eight elements (E_1–E_8).

The considered tool was positioned vertically in a water tank filled with water. The tank measured 5.0 m × 5.0 m × 4.0 m (length × width × height) and included an obstacle. A finite-length metal rod was placed vertically in the tank to simulate a target well (Fig. 26). The horizontal distance between the simulated target well and tool was 1.4 m, with the target well located at an azimuthal angle of 123° relative to the tool. The metal rod was moved vertically while keeping the tool fixed to simulate logging at different depths. The movement range extended from 3 to 1 m below the water surface (defined as 0 m depth), with a step size of 0.05 m, resulting in 41 depth positions. Throughout the process, the axis of the metal rod remained parallel to the tank wall.

5.2. Analysis of waveform characteristics

The received waveform data were obtained by raising the metal rod along the depth direction. Fig. 27 presents the

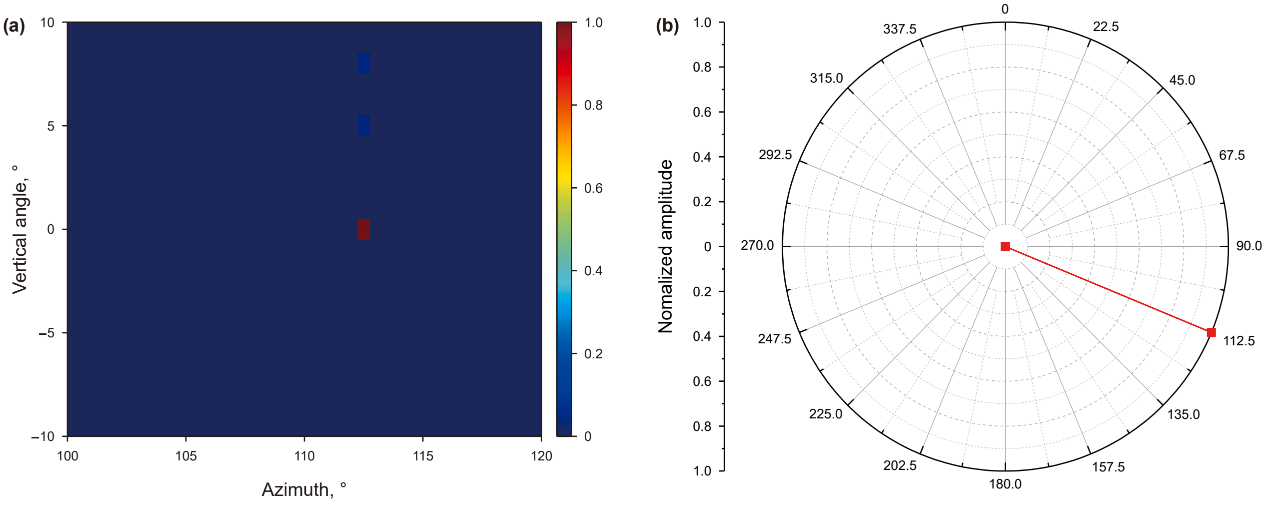

Fig. 14. (**a**) Azimuthal imaging of PP-wave echoes from an adjacent target well at $d = 1.0$ m; (**b**) normalized azimuthal localization curve.

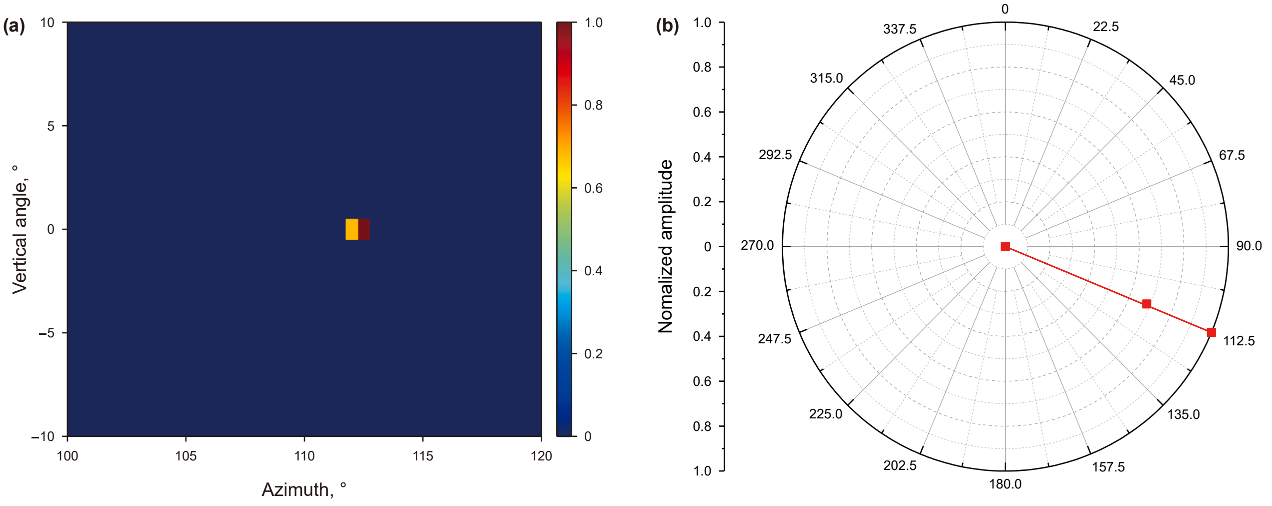

Fig. 15. (**a**) Azimuthal imaging of PP-wave echoes from an adjacent target well at $d = 15.0$ m; (**b**) normalized azimuthal localization curve.

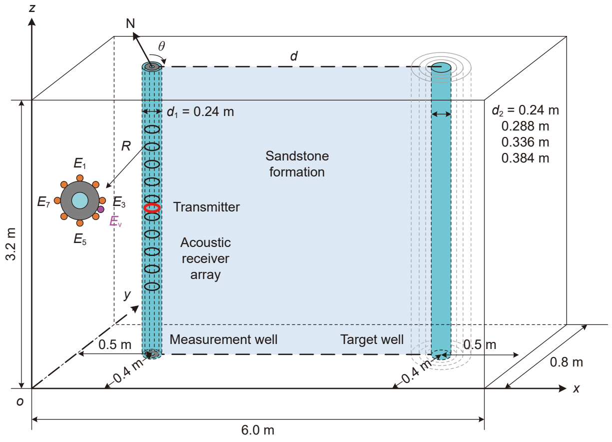

Fig. 16. Adjustment of the target well diameter to 1.0, 1.2, 1.4, and 1.6 times the initial diameter (0.24 m).

variable-density display of common-offset waveforms at different azimuths for the R_{-2} acoustic receiver station. The waveforms include direct waves, obstacle echoes, tank-wall echoes, and echoes from the simulated target well. Among these, the direct waves and obstacle echoes arrive earlier, followed by the echoes from the simulated target well at ~2 ms and then the tank-wall echoes. During the upward measurement, the spatial positions of the tool, obstacle, and tank wall remained fixed. Consequently, the tool's direct waves, as well as the obstacle and tank-wall echoes, were nearly identical across different depth points, resulting in linear patterns with depth variation. In contrast, as the simulated target well was a finite-length metal rod whose bottom end gradually approached the water surface as it was raised, its submerged length continuously changed. This caused the echoes from the simulated target well to vary at different depths, forming curved patterns with depth variation.

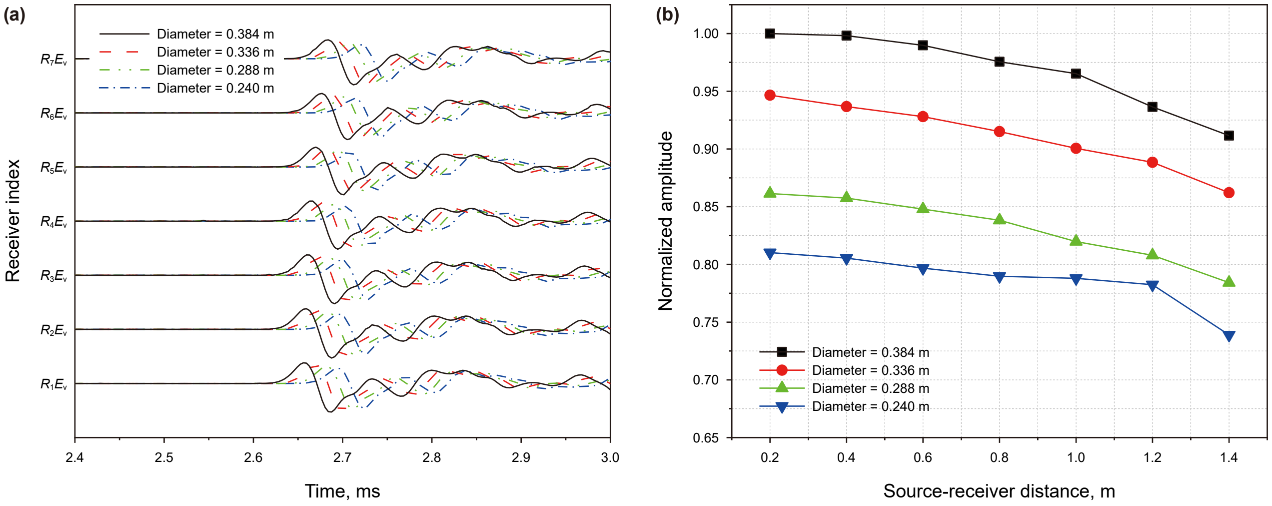

Fig. 17. (**a**) Echo waveforms at different source–receiver distances and (**b**) PP echo amplitudes as functions of source–receiver distance for target wells with different diameters.

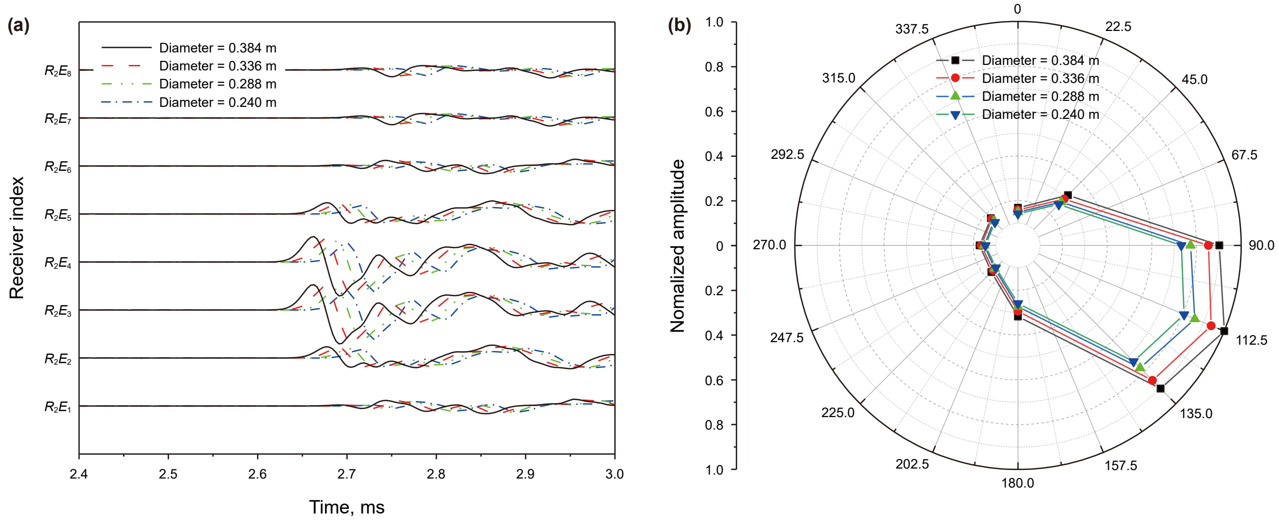

Fig. 18. Azimuthal dependences of (**a**) echo waveforms at receiver station R_2 and (**b**) PP echo amplitudes in target wells with different diameters.

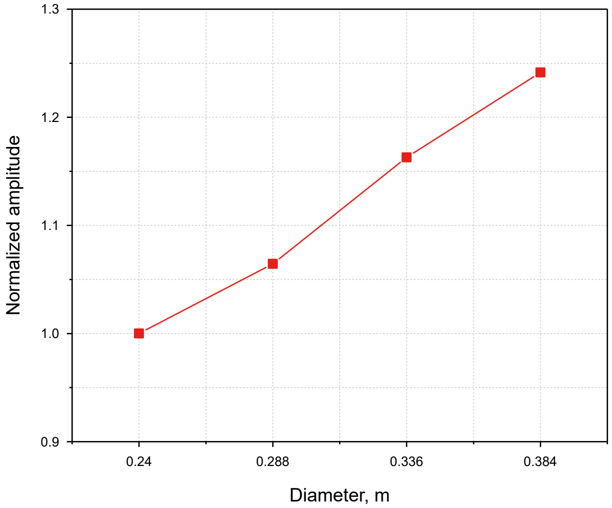

Fig. 19. PP echo amplitude versus target well diameter at receiving element R_2E_v.

Because the direct waves, obstacle echoes, and tank-wall echoes exhibit linear patterns (pertaining to changes in arrival times plotted against the depth), while the echoes from the simulated target well display curved ones, median filtering was applied along the depth direction to the waveforms in Fig. 27. This approach filtered out the former while preserving the latter. Fig. 28 shows the variable-density display of common-offset waveforms at different azimuths for the R_{-2} acoustic receiver station after median filtering. Evidently, the direct waves, obstacle echoes, and tank-wall echoes were considerably suppressed, whereas the echoes from the simulated target well were effectively preserved.

The single-shot waveform at the depth point of 1.85 m was selected for analysis (Fig. 29). The E_3 and E_4 receiver elements received earlier arrivals with stronger amplitudes. This is because the simulated target well was positioned at an azimuth of 123°, which directly faced the E_3 and E_4 elements. These observed characteristics closely match the echo

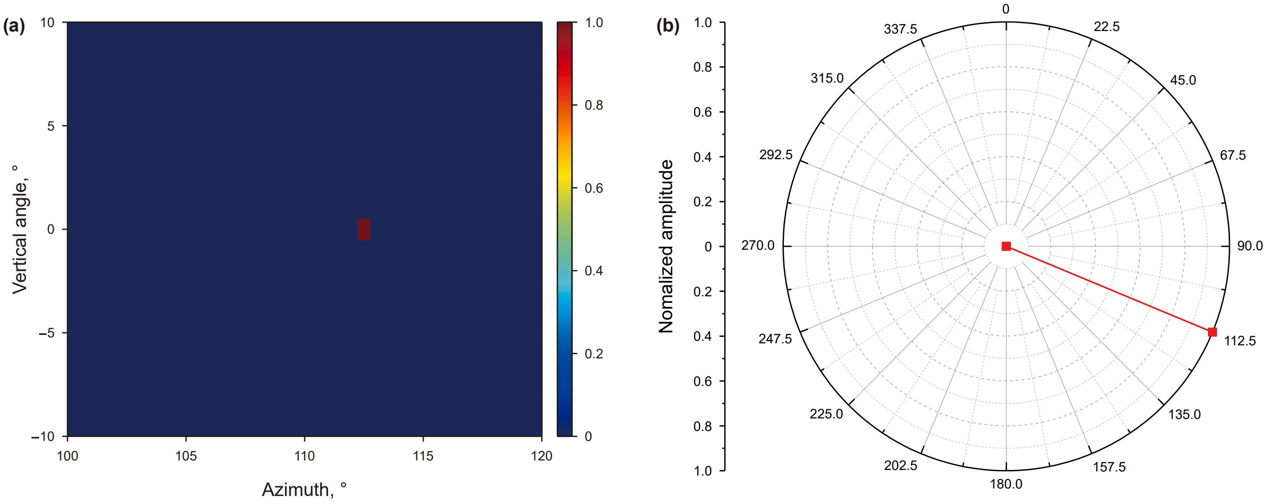

Fig. 20. **(a)** Azimuthal image of PP-wave echoes from an adjacent target well at $d = 5.0$ m and **(b)** normalized azimuthal localization curve for a target well with a diameter of 0.384 m (1.6 × initial diameter (0.24 m)).

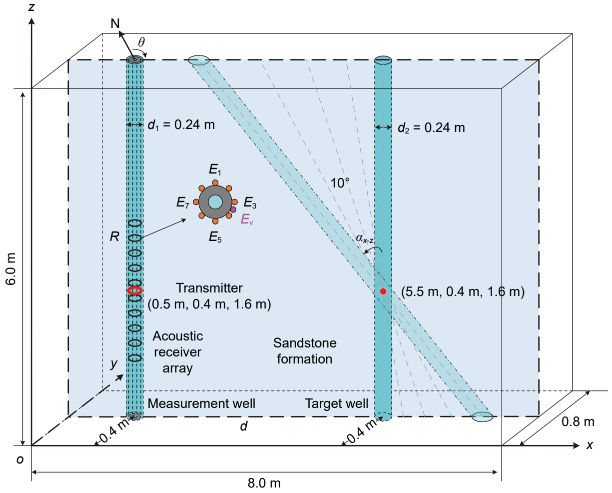

Fig. 21. Adjustment of relative angle α_{x-z} between the target and measurement wells.

waveform features of the target well obtained from numerical simulations.

5.3. Imaging processing

Based on the single-shot waveform at a depth of 1.85 m obtained after median filtering, azimuth imaging of the simulated target well was performed using the 3D-STC method (Bennett, 2019) and the CS method (Fig. 30(a) and (b), respectively). In Fig. 30(a), the maximum imaging point (black asterisk) corresponds to an azimuth angle of 127°. In Fig. 30(b), the maximum imaging point corresponds to an azimuth angle of 124°. Both results are close to the experimental reference value of 123°; however, the CS-based adjacent-well imaging method exhibits substantially higher azimuthal resolution. Both the imaging methods were employed for processing single-shot waveform data from 41 depth points within a depth range of 1–3 m, and the normalized azimuth positioning curves of the simulated target well were extracted at each depth point. Fig. 31 shows the resulting azimuthal images of the simulated target well at these 41 depth points. The multidepth-point azimuth calculation results are summarized in Table 2. Both the methods inverted azimuth angles close to the actual value of 123°; however, the 3D-STC method showed a larger standard deviation in azimuth calculations compared to the CS method. The latter consistently demonstrated superior azimuthal resolution. Thus, the adjacent-well imaging method based on CS shows high feasibility in practical applications.

6. Discussion

To further evaluate the applicability of the CS-based adjacent-well imaging method in strong-noise environments, we adjusted the median-filtering parameters and applied depth-direction median filtering to the waveforms shown in Fig. 27. This produced waveforms with partially filtered direct waves, obstacle echoes, and tank-wall echoes are shown in Fig. 32, where considerable residual noise remained in the waveforms. Based on single-shot waveforms at different depth points, the azimuth imaging results of the simulated target well obtained using the 3D-STC and CS methods are shown in Fig. 33(a) and (b), respectively. The multidepth-point azimuth calculation results are summarized in Table 3. Even with high-amplitude noise in the waveforms, both methods produced inverted azimuth angles for the simulated target well that were close to the real value of 123°, with a standard deviation of <5° in azimuth angle calculations. Furthermore, the CS method maintained superior azimuth resolution compared to the 3D-STC method.

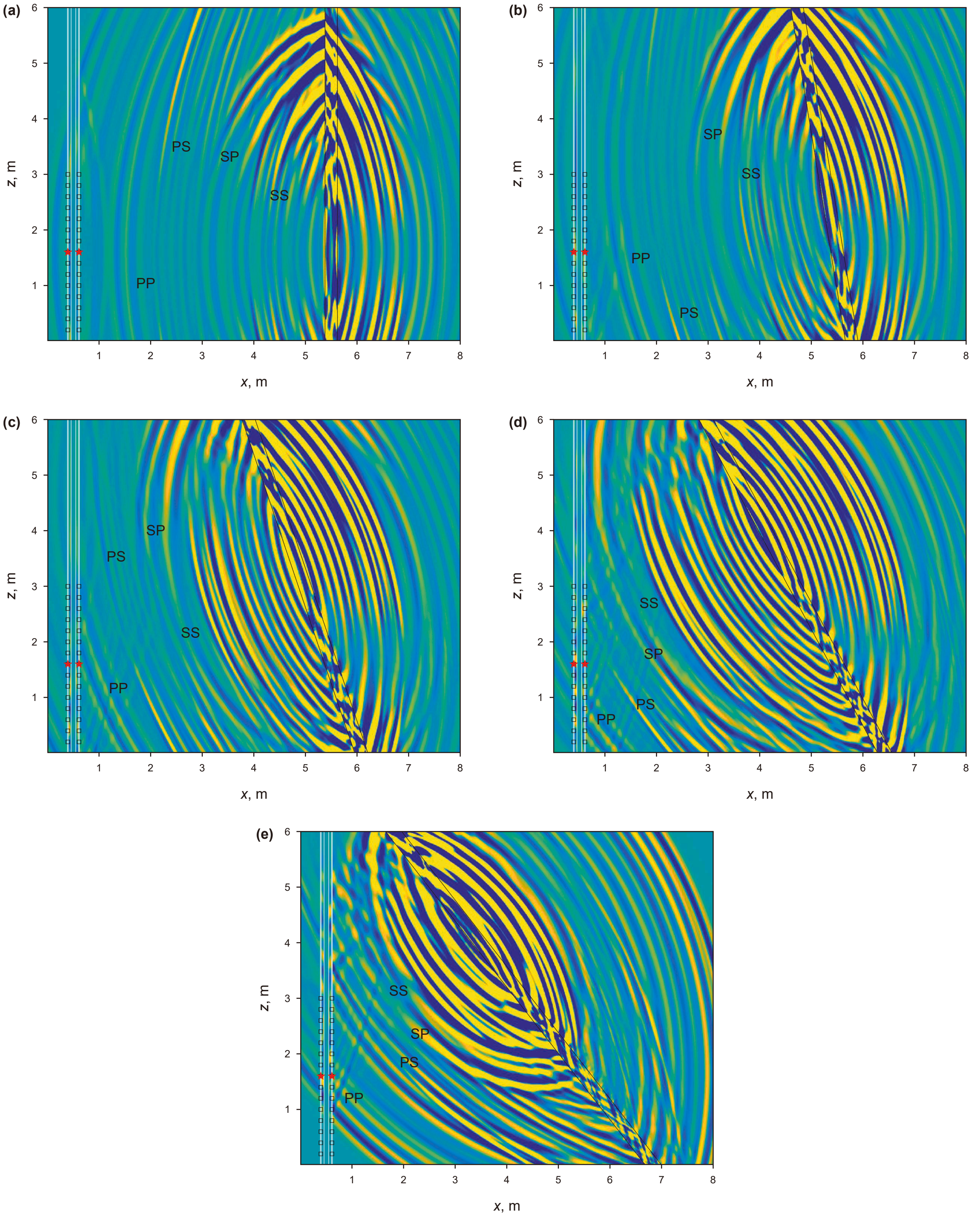

Fig. 22. Snapshots of echo wavefields at different relative angles $\alpha_{x\text{–}z}$ between the target and measurement wells: **(a)** 0°, **(b)** 10°, **(c)** 20°, **(d)** 30°, and **(e)** 40°. The solid black lines mark the boundary of the target borehole.

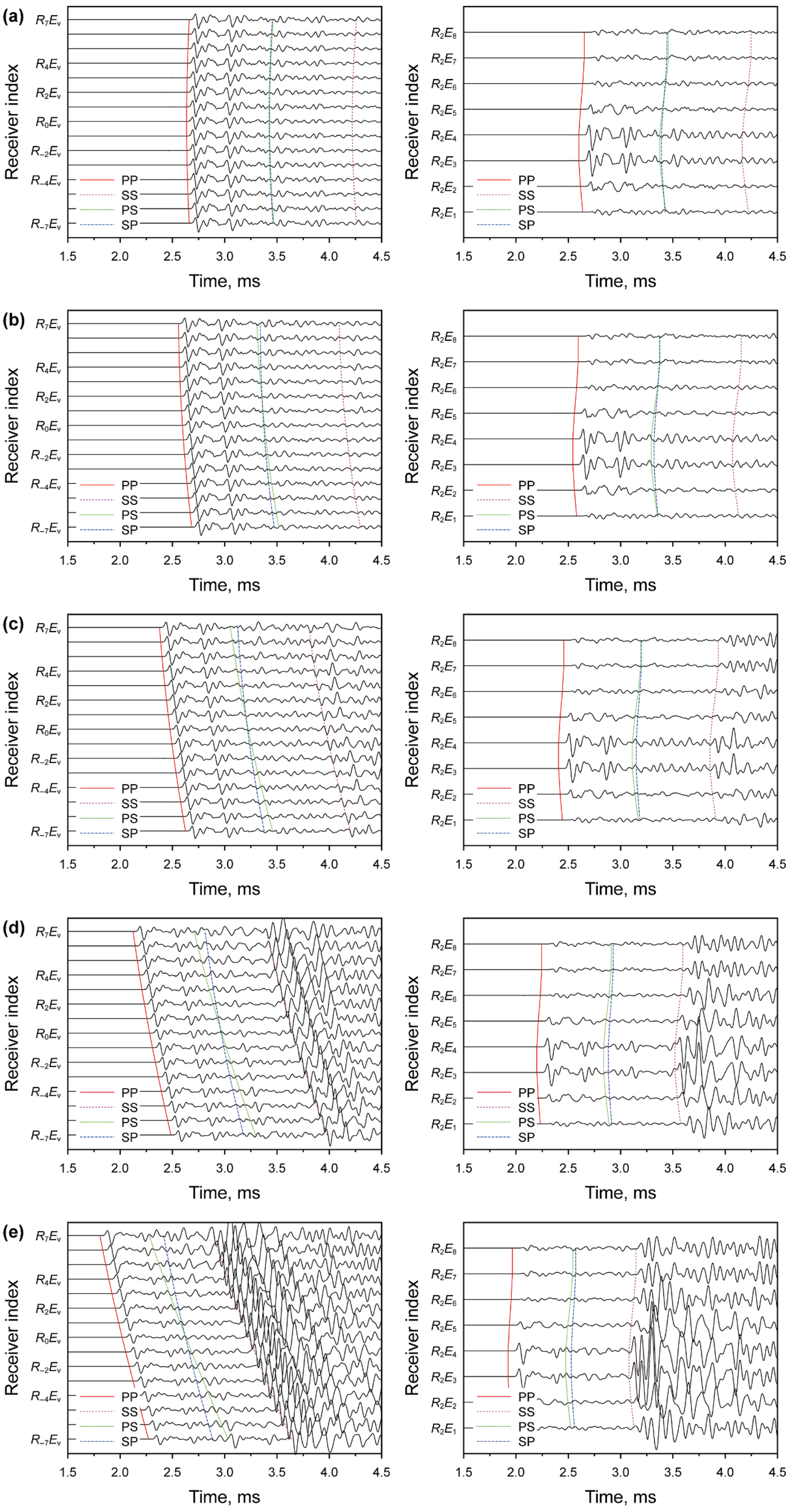

Fig. 23. Echo waveforms at different relative angles $\alpha_{x\text{–}z}$ between the target and measurement wells: **(a)** 0°, **(b)** 10°, **(c)** 20°, **(d)** 30°, and **(e)** 40°.

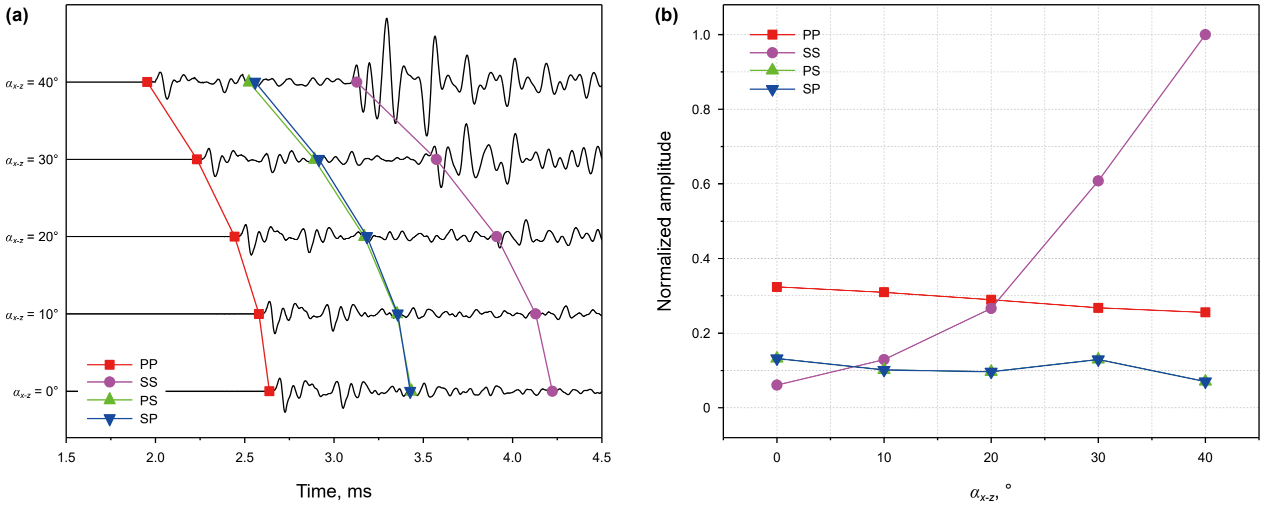

Fig. 24. **(a)** Echo waveforms and **(b)** echo amplitudes versus relative angle $\alpha_{x\text{–}z}$ of different echo modes at receiver element R_2E_v.

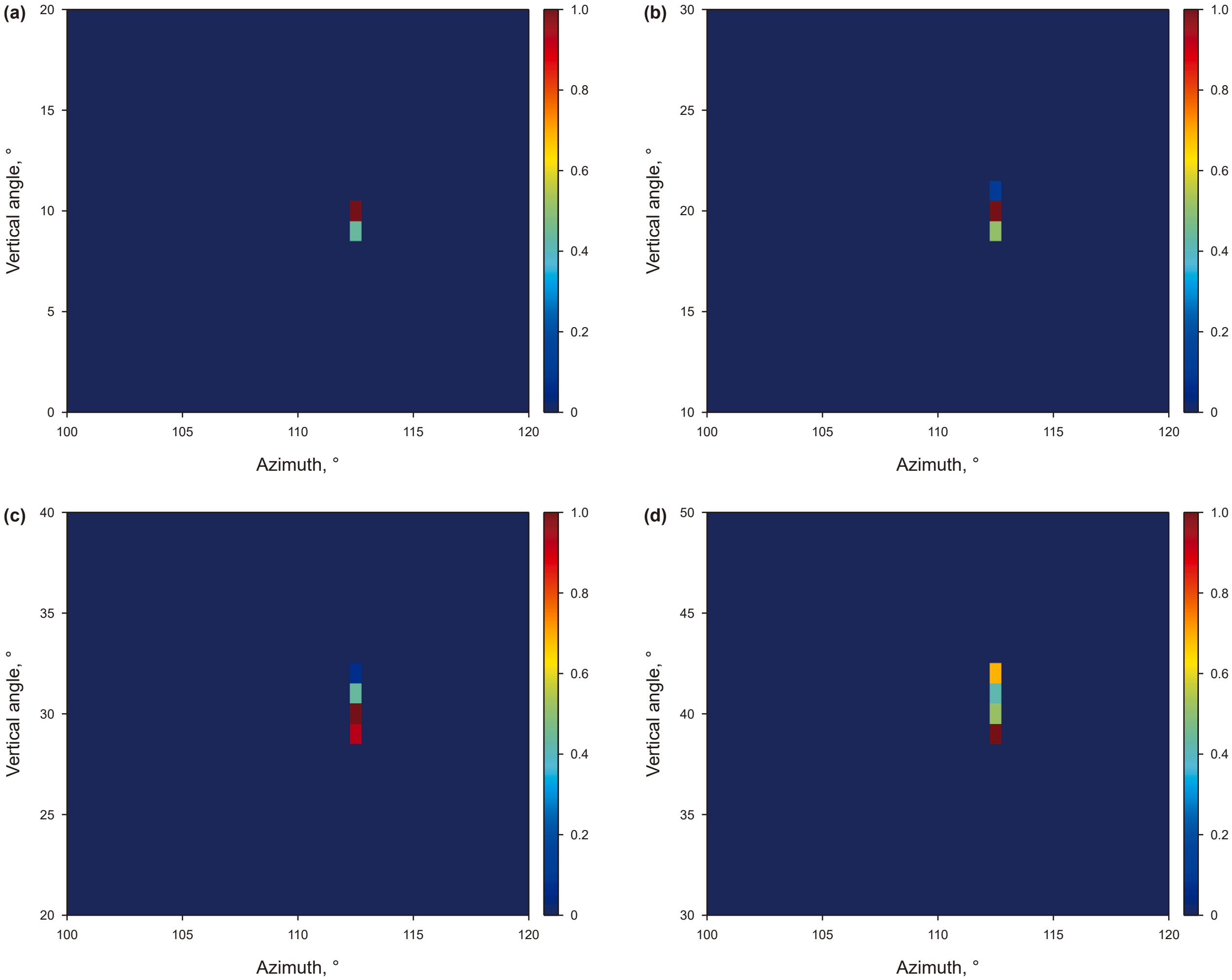

Fig. 25. Azimuthal imaging of an adjacent target well near the measurement borehole: PP-wave images at **(a)** $\alpha_{x\text{–}z} = 10°$ and **(b)** $\alpha_{x\text{–}z} = 20°$; SS-wave images at **(c)** $\alpha_{x\text{–}z} = 30°$ and **(d)** $\alpha_{x\text{–}z} = 40°$.

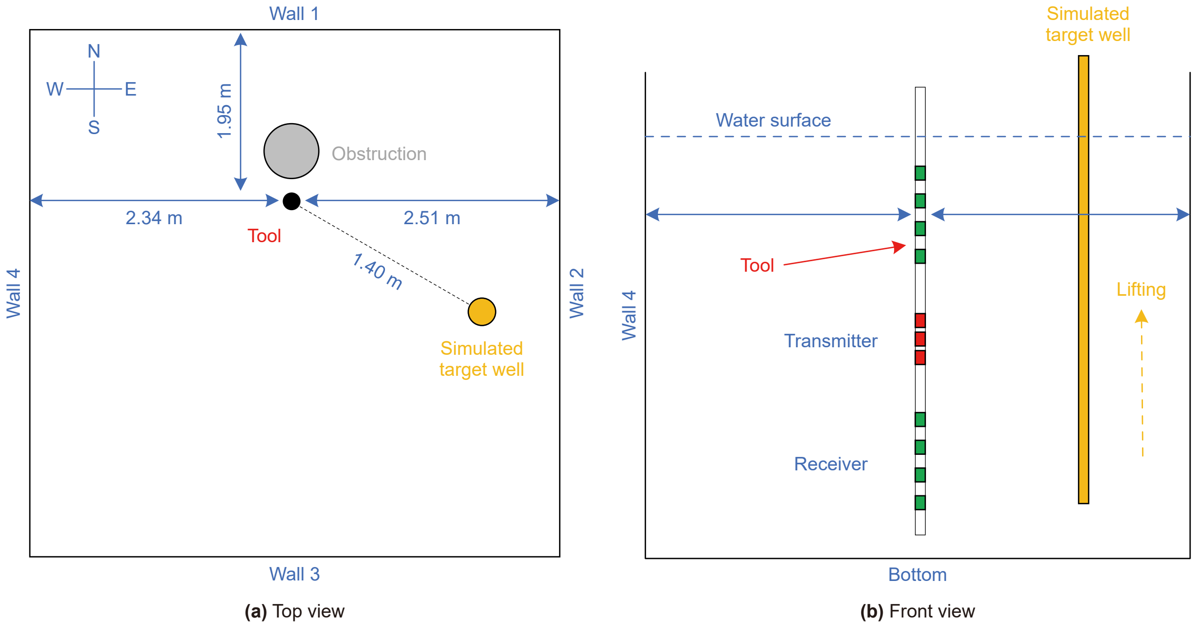

Fig. 26. Schematic of the physical simulation experiment.

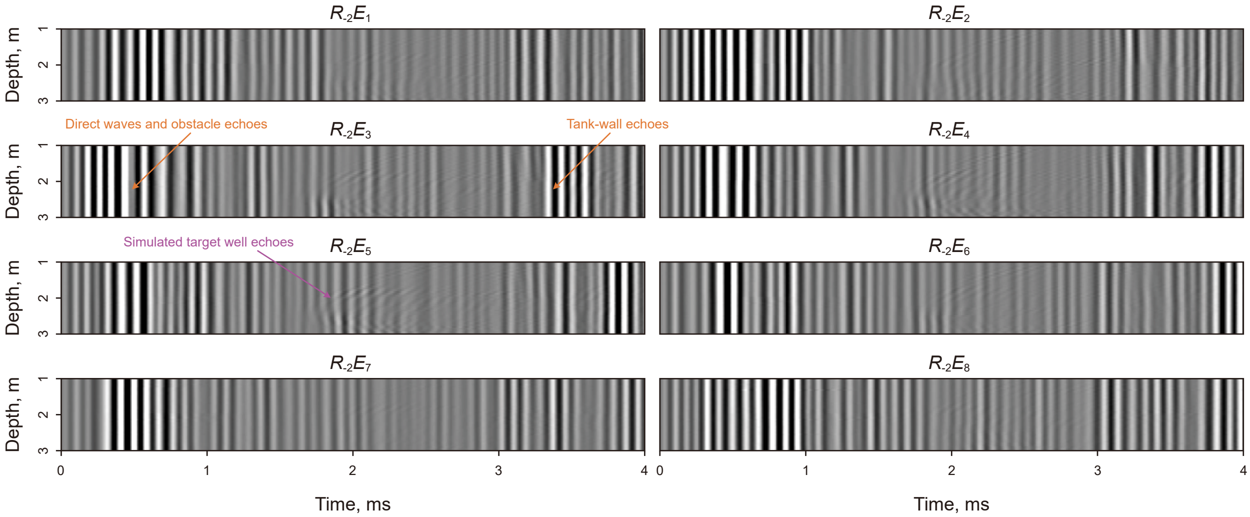

Fig. 27. Variable-density displays of common-offset waveforms from different azimuths at the R_{-2} acoustic receiver station.

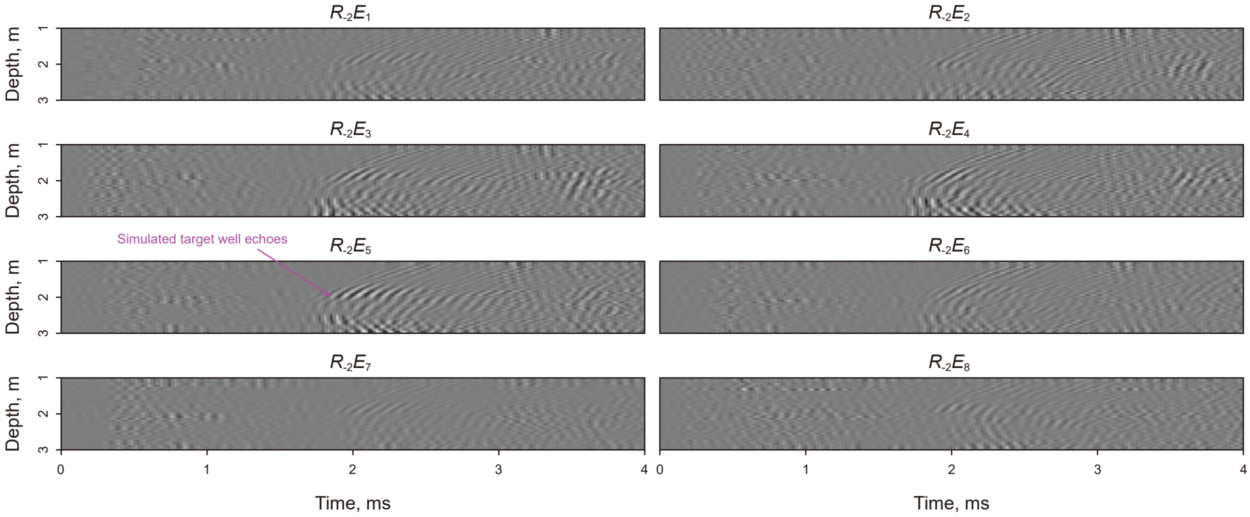

Fig. 28. Variable-density displays of common-offset waveforms from different azimuths at the R_{-2} acoustic receiver station after median-filtering processing.

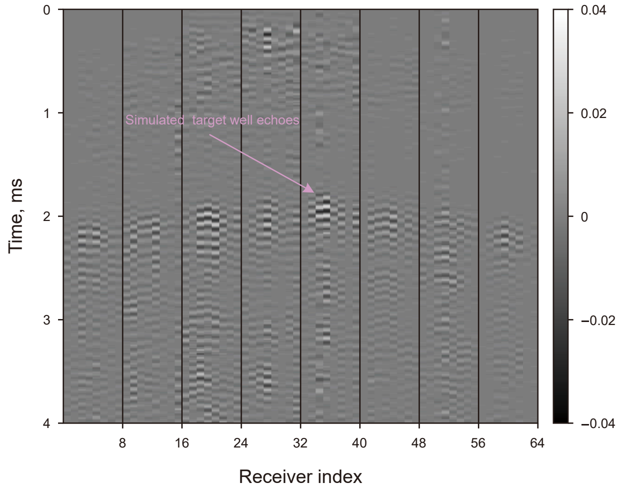

Fig. 29. Variable-density display of single-shot waveforms at depth point 1.85 m. Receiver elements are numbered in order of their azimuthal variation *E* followed by their source-to-receiver distance *R*: $R_{-4}E_1$–$R_{-4}E_8$, …, $R_{-1}E_1$–$R_{-1}E_8$, R_1E_1–R_1E_8, …, R_4E_1–R_4E_8.

Table 2
Azimuth calculation results for multiple depth points obtained using different methods.

	3D-STC	CS
Mean value	122°	122°
Standard deviation	2.52°	1.91°

In the physical simulation experiment, a finite-length metal rod was vertically placed in a water tank to simulate the target well. This approach reduced the operational complexity of the simulation and produced favorable adjacent-well imaging results. However, differences in acoustic properties exist between the metal rod and actual open or cased boreholes. Additionally, the water-tank experiment cannot fully replicate the modulation effects of boreholes on acoustic radiation and reception. As a next step, we plan to deploy adjacent-well-acoustic-detection-while-drilling tools in actual boreholes to detect adjacent target wells, enabling the acquisition of field data for adjacent-well acoustic detection while drilling, followed by processing and imaging verification.

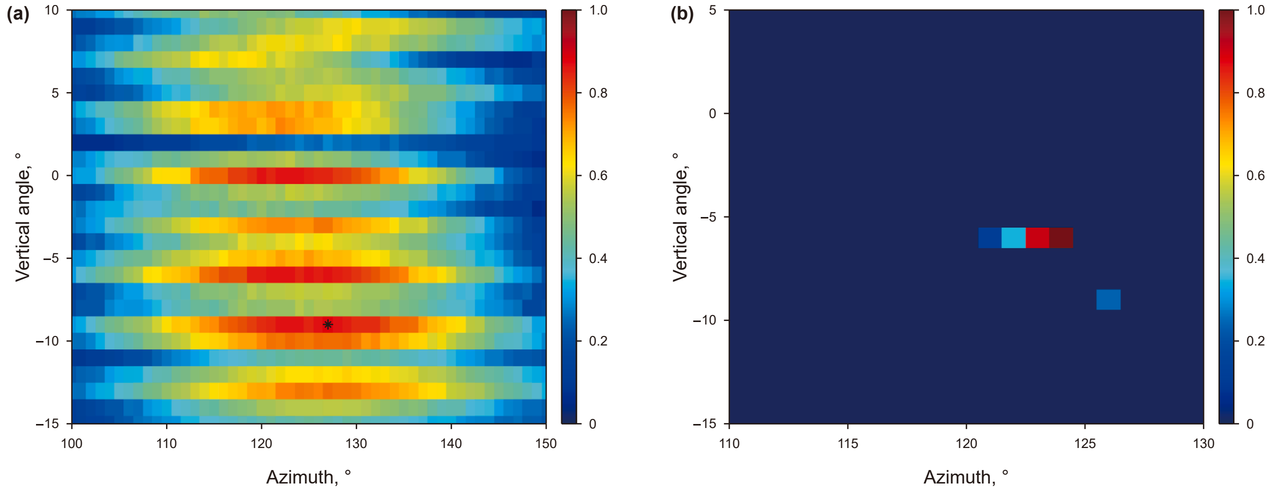

Fig. 30. Azimuth imaging results of the simulated target well derived from the single-shot waveforms at 1.85 m depth, obtained via the **(a)** 3D-STC and **(b)** CS methods.

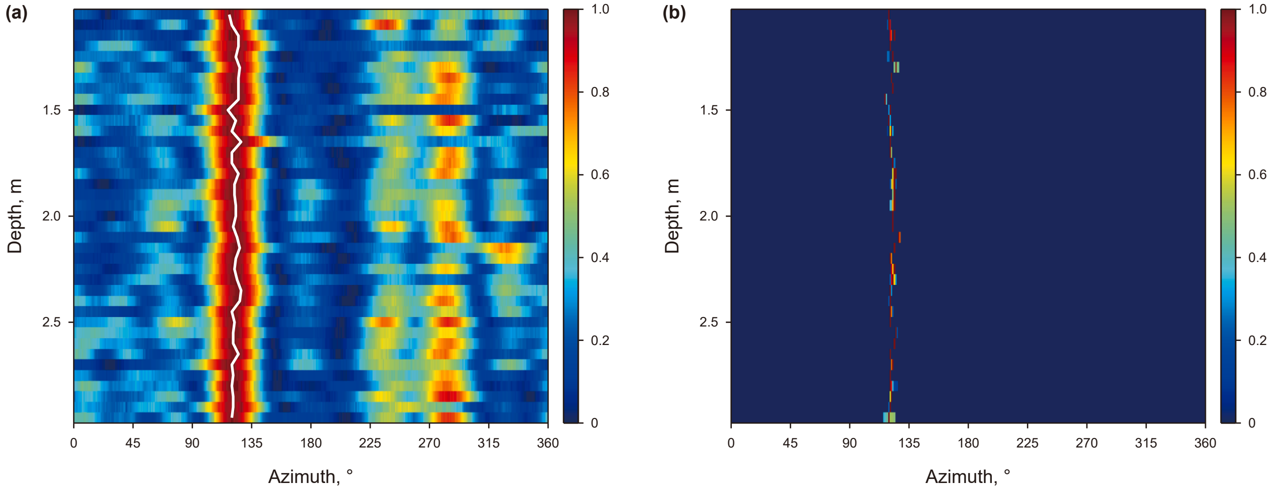

Fig. 31. Azimuth imaging results of the simulated target well at different depth points obtained via the **(a)** 3D-STC and **(b)** CS methods.

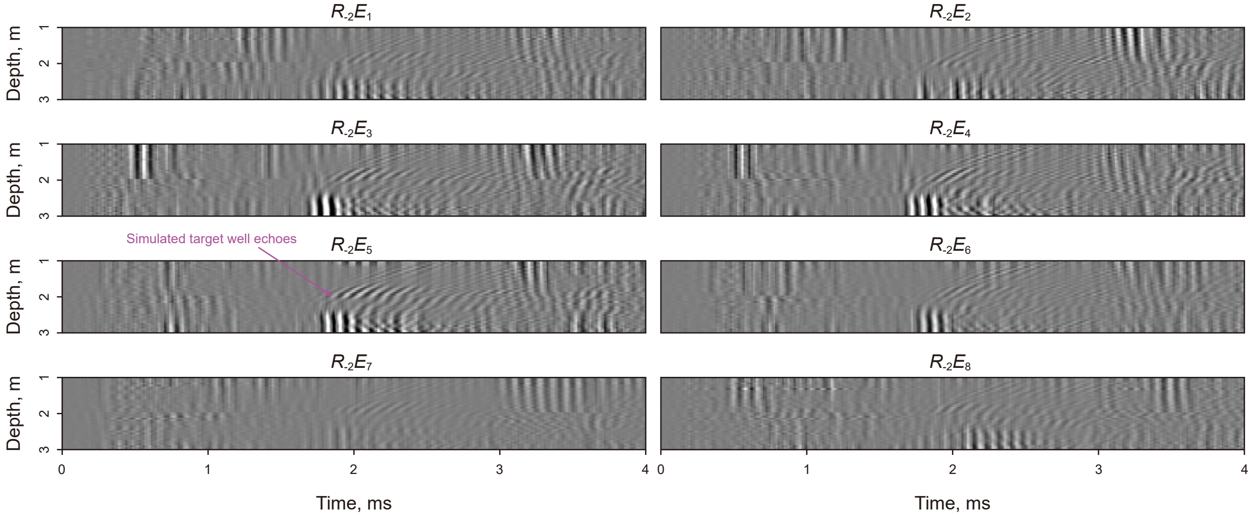

Fig. 32. Variable-density displays of common-offset waveforms obtained from different azimuths at the R_{-2} acoustic receiver station after median filtering, showing residual noise.

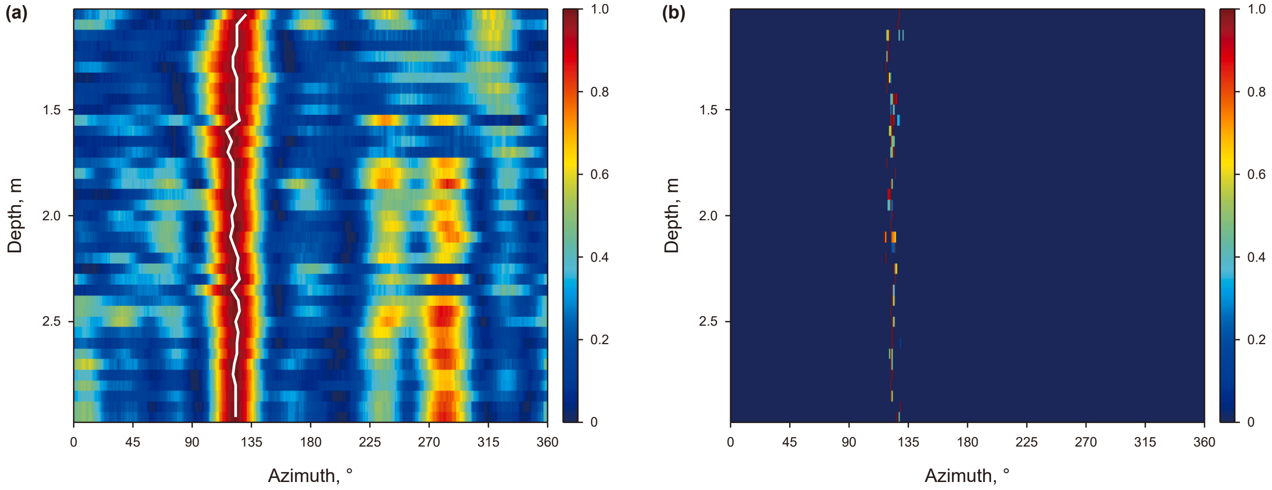

Fig. 33. Azimuth imaging results of the simulated target well at different depth points obtained through the **(a)** 3D-STC and **(b)** CS methods in the presence of residual noise.

Table 3
Azimuth calculation results at multiple depth points obtained using different methods in the presence of residual noise.

	3D-STC	CS
Mean value	122°	122°
Standard deviation	2.67°	2.59°

7. Conclusions

Herein, an adjacent-well-acoustic-detection-while-drilling method and an adjacent-well imaging method based on CS were proposed. These methods were first evaluated using 3D finite-difference simulations under drilling conditions for two scenarios: with and without a target well adjacent to the measurement well. The target well was imaged using compressive sensing. Subsequently, the practicality of these methods was validated through preliminary water-tank experiments. The key conclusions of this study are as follows:

(1) The linear phased array source generates P- and S-waves in near-borehole formations, exhibiting vertically symmetric radiation patterns with distinct directional characteristics: As the P-wave energy is horizontally concentrated at low vertical angles, it is optimal for detecting target wells that are parallel or subparallel to the borehole. Conversely, the S-wave energy approaches zero in the horizontal direction and is concentrated at medium-to-high vertical angles, making it more effective for detecting target wells at large inclination angles relative to the borehole.

(2) Increased radial distance from the target well extends the PP-wave propagation delay, attenuates PP-wave amplitude, and promotes a gradual transition to plane-wave characteristics. In contrast, linear expansion of the borehole diameter reduces the PP-wave time of flight while amplifying PP-wave signal strength. Detection efficacy depends on the alignment of the wells: PP echoes yield better results at small inclination angles (near-parallel wells), whereas SS echoes are more effective at large inclination angles. Across

all wave modes, the receiving element closest to the azimuth of the target well records the strongest signal and the earliest arrival time.

(3) The adjacent-well imaging method based on CS achieves very high spatial resolution. In single-shot azimuthal images, target wells appear as local maximum-intensity points. The positions of these maxima accurately reflect the azimuth of the target wells and allow estimation of the relative angle between the target and measurement wells. In the physical simulation experiments, the simulated target well was clearly imaged at various depth points and the inverted azimuth closely matched the actual experimental values. These results indicate that the CS-based adjacent-well imaging method offers a promising approach for locating target wells near measurement wells under real drilling conditions.

These findings demonstrate the successful integration of wireline borehole acoustic reflection imaging with drilling technology, offering enormous theoretical and engineering implications for real-time drilling operations.

CRediT authorship contribution statement

Teng Zhao: Writing – review & editing, Writing – original draft, Software, Methodology, Investigation, Conceptualization. **Gen-Sheng Li:** Writing – review & editing, Supervision, Resources, Funding acquisition, Conceptualization. **Xiao-Hua Che:** Writing – review & editing, Validation. **Wen-Xiao Qiao:** Writing – review & editing, Validation. **Jun-Qiang Lu:** Writing – review & editing, Validation. **Bai-Yong Men:** Writing – review & editing, Validation.

Declaration of competing interests

The authors declare that they have no known competing financial interests or personal relationships that could have appeared to influence the work reported in this paper.

Acknowledgements

This work was supported in part by the National Natural Science Foundation of China under Grant Nos. 12334019, 12274465, 12504558 and U25B20244 and in part by the China Postdoctoral Science Foundation under Grant No. 2025M770469 and in part by the Postdoctoral Fellowship Program of CPSF under Grant No. GZC20251952 and in part by the Science Foundation of China University of Petroleum, Beijing under Grant No. 2462025XKBH014.

References

Al-Muhailan, M., Al-Saleh, A., Al-Shayji, A.K., Rajagopalan, A., McKinnell, D.C., 2014. Directional challenges and planning of relief well to resolve an HP/HT well blowout. In: The IADC/SPE Drilling Conference and Exhibition, SPE167984.

Ben, J.L., Qiao, W.X., Che, X.H., Ju, X.D., Lu, J.Q., Men, B.Y., 2020. Field validation of imaging an adjacent borehole using scattered P-waves. Pet. Sci. 17 (5), 1272–1280. https://doi.org/10.1007/s12182-020-00475-5.

Bennett, N.N., 2019. 3D slowness time coherence for sonic imaging. Geophysics 84 (5), D179–D189. https://doi.org/10.1190/geo2018-0077.1.

Candes, E.J., Romberg, J., Tao, T., 2006. Robust uncertainty principles: Exact signal reconstruction from highly incomplete frequency information. IEEE Trans. Inform. Theory. 52 (2), 489–509. https://doi.org/10.1109/tit.2005.862083.

Candes, J., 2008. The restricted isometry property and its implications for compressed sensing. C. R. Math. 346, 589–592.

Chai, Y., Zhang, W.R., Wang, G.Q., Liu, J.D., Xu, M., Liu, D.D., Song, C.L., 2009. Application of remote exploration acoustic reflection imaging logging technique in fractured reservoir. Well Logging Technol. 33, 539–543. https://doi.org/10.16489/j.issn.1004-1338.2009.06.017 (in Chinese).

Che, X.H., Qiao, W.X., Ju, X.D., Lu, J.Q., Wu, J.P., Cai, M., 2016. Experimental study of the azimuthal performance of 3D acoustic transmitter stations. Pet. Sci. 13 (1), 52–63. https://doi.org/10.1007/s12182-015-0073-2.

Chu, N., Picheral, J., Mohammad-Djafari, A., Gac, N., 2014. A robust super-resolution approach with sparsity constraint in acoustic imaging. Appl. Acoust. 76, 197–208. https://doi.org/10.1016/j.apacoust.2013.08.007.

Donoho, D.L., 2006. Compressed sensing. IEEE Trans. Inform. Theory 52, 1289–1306. https://doi.org/10.1109/tit.2006.871582.

Edelmann, G.F., Gaumond, C.F., 2011. Beamforming using compressive sensing. J. Soc. Am. 130, EL232–EL237. https://doi.org/10.1121/1.3632046.

Gao, D.L., Diao, B.B., Yu, R.F., Zhang, S., 2023. Research advances in magnetic guidance drilling technique for relief well engineering. J. China Univ. Pet. 47, 55–64. https://doi.org/10.3969/j.issn.1673-5005.2023.05.006 (in Chinese).

Gong, H., Chen, H., He, X., Wang, X., 2015. Eliminating the azimuth ambiguity in single-well imaging using 3C sonic data. Geophysics 80 (1), A13–A17. https://doi.org/10.1190/geo2014-0337.1.

Grills, T.L., 2002. Magnetic ranging technologies for drilling steam assisted gravity drainage well pairs and unique well geometries – A comparison of technologies. In: The SPE International Thermal Operations and Heavy Oil Symposium and International Horizontal Well Technology Conference, SPE-79005.

Gu, X.H., Tang, X.M., Su, Y.D., 2021. Delineating a cased borehole in unconsolidated formations using dipole acoustic data from a nearby well. Geophysics 86 (5), D139–D147. https://doi.org/10.1190/geo2020-0570.1.

Gu, X.H., Tang, X.M., Su, Y.D., Li, S.Q., 2025. Acoustic ranging of multiple nearby wells using dipole acoustic logging. Geophysics 90 (2), A15–A19. https://doi.org/10.1190/geo2024-0621.1.

Hanak, F.C., Estes, R., 2015. High speed, continuous single well magnetic ranging. In: The SPE/IADC Drilling Conference and Exhibition pp. D011S006R003.

Hirabayashi, N., 2021. Beamform processing for sonic imaging using monopole and dipole sources. Geophysics 86 (1), D1–D14. https://doi.org/10.1190/geo2020-0235.1.

Hornby, B.E., 1989. Imaging of near-borehole structure using full-waveform sonic data. Geophysics 54 (6), 747–757. https://doi.org/10.1190/1.1442702.

Huggins, P.S., Zucker, S.W., 2007. Greedy basis pursuit. IEEE Trans. Signal Process. 55 (7), 3760–3772. https://doi.org/10.1109/tsp.2007.894287.

Jervis, M., Tonellot, T., Bakulin, A., Ghamdi, I.A., 2018. High-resolution acoustic imaging from a borehole to detect a nearby well. Lead. Edge 37 (1), 812–817. https://doi.org/10.1190/tle37110812.

Johansen, A.L., Allen, W.T., Goobie, R., Bennett, N., Poedjono, B., Calvez, J.L., 2019. Advances in active acoustic ranging. Lead. Edge 38 (11), 843–849. https://doi.org/10.1190/tle38110843.1.

Kong, F.T., Liu, Y.X., Gu, X.H., Zhen, L., Luo, C.M., Li, S.Q., 2024. Extraction of reflected waves from acoustic logging data using variation mode decomposition and curvelet transform. Pet. Sci. 21 (5), 3142–3156. https://doi.org/10.1016/j.petsci.2024.05.017.

Kuckes, A.F., Hay, R.T., McMahon, J., Nord, A.G., Schilling, D.A., Morden, J., 1996. New electromagnetic surveying/ranging method for drilling parallel horizontal twin wells. SPE Drill. Complet. 11 (2), 85–90. https://doi.org/10.2118/27466-pa.

Lane, J.B., Wesson, J.P., 1992. Magnetic ranging tool accurately guides replacement well. Oil Gas J. 90.

Li, C., Chen, H., He, X., Wang, X., 2021. Identifying reflector azimuth from borehole multicomponent cross-dipole acoustic measurement. Geophysics 86 (6), D201–D214. https://doi.org/10.1190/geo2020-0460.1.

Li, G.S., Song, X.Z., Tian, S.C., Zhu, Z.P., 2022a2022. Intelligent drilling and completion: A review. Engineering 18, 33–48. https://doi.org/10.1016/j.eng.2022.07.014.

Li, G.S., Wu, X.G., Song, X.Z., Zhou, S., Li, M., Zhu, H., Kong, Y., Huang, Z., 2022b2022. Status and challenges of hot dry rock geothermal resource exploitation. Pet. Sci. Bull. 7, 343–364 (in Chinese).

Li, Z., Lee, S.Q., Qi, Q.M., Su, Y.D., Wang, X.J., 2022c2022. Investigation of through-casing borehole acoustic reflection imaging with a dipole source: Modeling and field application. J. Nat. Gas Sci. Eng. 105, 104715. https://doi.org/10.1016/j.jngse.2022.104715.

Li, Z., Qi, Q., Hei, C., Jiang, C., Wang, X.-J., 2022d2022. Elastic-wave radiation, scattering, and reception of a dipole acoustic logging-while-drilling source in unconsolidated formations. Front. Earth Sci. 10, 879345. https://doi.org/10.3389/feart.2022.879345.

Liu, X., Zhao, T., Che, X., 2023. Preliminary numerical simulation of acoustic reflection imaging logging while drilling based on the vertical incidence of acoustic waves on the borehole wall. Well Logging Technol 47, 542–550. https://doi.org/10.16489/j.issn.1004-1338.2023.05.003 (in Chinese).

Liu, P., Fan, H.-J., Zhang, M.-S., Li, Z., Jiang, J.-W., Gao, Y., Wang, K.-W., 2025. Response characteristics of shear waves scattered by fractures with borehole observation system. Pet. Sci. 22 (5), 1912–1928. https://doi.org/10.1016/j.petsci.2025.03.004.

Lustig, M., Donoho, D.L., Santos, J.M., Pauly, J.M., 2008. Compressed sensing MRI. IEEE Signal Process. Mag. 25, 72–82. https://doi.org/10.1109/msp.2007.914728.

Massa, A., Rocca, P., Oliveri, G., 2015. Compressive sensing in electromagnetics – A review. IEEE Antenn. Propag. Mag. 57 (1), 224–238. https://doi.org/10.1109/map.2015.2397092.

Needell, D., Vershynin, R., 2010. Signal recovery from incomplete and inaccurate measurements via regularized orthogonal matching pursuit. IEEE J. Sel. Top. Signal Process 4, 310–316. https://doi.org/10.1109/jstsp.2010.2042412.

Niu, D.C., Su, Y.D., 2022. Adjacent borehole imaging method based on acoustic remote detection in shallow unconsolidated formations. Pet. Drill. Tech. 50, 21–27. https://doi.org/10.11911/syztjs.2022111 (in Chinese).

Poedjono, B., Alatrach, S., Martin, A., Goobie, R.B., Allen, W.T., Sweeney, E., 2017. Active acoustic ranging to locate two nearby wellbores in deepwater Gulf of Mexico. In: SPE Annual Technical Conference and Exhibition,. D021S015R001.

Qian, R.J., 2010. Classification studies on seismic resolution and migration's affect to resolution. Oil Geophys. Prospect. 45, 306–313. https://doi.org/10.13810/j.cnki.issn.1000-7210.2010.02.015 (in Chinese).

Qiao, W.X., Ju, X.D., Che, X.H., Lu, J.Q., 2011. Transducers and acoustic well logging technology. Physics 40, 99–106 (in Chinese).

Simard, P., Antoni, J., 2013. Acoustic source identification: experimenting the $\ell 1$ minimization approach. Appl. Acoust. 74 (7), 974–986. https://doi.org/10.1016/j.apacoust.2013.01.012.

Song, X.Z., Li, G.S., Wang, G.S., Yang, R., 2022. Research progress on heat extraction technology for developing medium-deep geothermal energy. Sci. Technol. Rev. 40, 42–51. https://doi.org/10.3981/j.issn.1000-7857.2022.20.006 (in Chinese).

Su, Y.D., Wei, Z.T., Tang, X.M., 2014. A validation method of dipole shear-wave remote reflection imaging from adjacent borehole reflection. J. Appl. Acoust. 33, 29–34. https://doi.org/10.11684/j.issn.1000-310X.2014.01.005 (in Chinese).

Tang, X., Cao, J., Li, Z., Su, Y., 2016. Detecting a fluid-filled borehole using elastic waves from a remote borehole. J. Acoust. Soc. Am. 140, EL211–EL217. https://doi.org/10.1121/1.4960143.

Tang, X.M., 2004. Imaging near-borehole structure using directional acoustic-wave measurement. Geophysics 69 (6), 1378–1386. https://doi.org/10.1190/1.1836812.

Tropp, J.A., Gilbert, A.C., 2007. Signal recovery from random measurements via orthogonal matching pursuit. IEEE Trans. Inform. Theory 53, 4655–4666. https://doi.org/10.1109/tit.2007.909108.

Varela, R., Iturrizaga, F., Patino, D., Atencio, N., Romero, D., Buitrago, O., Pineda, J., 2015. Multiple relief well planning for an HPHT blowout in Southern Mexico. In: SPE/IADC Drilling Conference and Exhibition, SPE-173160-MS.. https://doi.org/10.2118/173160-MS.

Wang, L., Deng, S.-G., Zhang, P., Cao, Y.C., Fan, Y.R., Yuan, X.Y., 2019. Detection performance and inversion processing of logging-while-drilling extra-deep azimuthal resistivity measurements. Pet. Sci. 16 (5), 1015–1027. https://doi.org/10.1007/s12182-019-00374-4.

Wang, L., Li, S., Fan, Y., 2020. An all-new ultradeep detection method based on hybrid dipole antennas in electromagnetic logging while drilling. IEEE Trans. Geosci. Remote Sens. 58 (3), 2124–2134. https://doi.org/10.1109/tgrs.2019.2953304.

Wang, L., Deng, S.G., Xie, G.B., Li, S.J., Wu, Z.G., Fan, Y.R., 2022. A new deep-reading look-ahead method in electromagnetic logging-while-drilling using the scattered electric field from magnetic dipole antennas. Pet. Sci. 19 (1), 180–188. https://doi.org/10.1016/j.petsci.2021.09.035.

Wang, T.Y., Li, G.S., Song, X.Z., Wang, H., Wang, G., Liu, Z., 2024. Development of smart oil and gas fields with multi-energy synergy of wind, solar, geothermal, and energy storage. Strateg. Study CAE 26, 259–270. https://doi.org/10.15302/j-sscae-2024.04.004 (in Chinese).

Xenaki, A., Gerstoft, P., Mosegaard, K., 2014. Compressive beamforming. J. Acoust. Soc. Am. 136, 260–271. https://doi.org/10.1121/1.4883360.

Xu, J., Hu, H., Wang, Z., 2019. Asymptotic solution to a 3D dipole single-well imaging system with combined monopole and dipole receivers with an application in elimination of azimuth ambiguity. Geophysics 84 (1), D191–D207. https://doi.org/10.1190/geo2018-0658.

Zhang, Y., Zhang, L.Y., Zhou, J., Liu, L., Chen, F., He, X., 2016. A review of compressive sensing in information security field. IEEE Access 4, 2507–2519. https://doi.org/10.1109/ACCESS.2016.2569421.

Zhang, S., Diao, B., Gao, D., 2020. Numerical simulation and sensitivity analysis of accurate ranging of adjacent wells while drilling. J. Pet. Sci. Eng. 195, 107536. https://doi.org/10.1016/j.petrol.2020.107536.

Zhao, T., Che, X., Qiao, W., Cheng, L., 2023. Borehole azimuthal acoustic imaging using 3D spatial scanning: application in acoustic detection of nearby wells. Geophysics 88 (2), D131–D145. https://doi.org/10.1190/geo2022-0376.1.

Zhao, L., Li, Z., Guo, S.J., Sun, X.F., 2024a. Research on the application of acoustic far detection technology in relief well. Well Logging Tech 48, 248–255. https://doi.org/10.16489/j.issn.1004-1338.2024.02.013 (in Chinese).

Zhao, T., Che, X., Qiao, W., 2024b. Azimuth estimation method for borehole acoustic reflection imaging using an acoustic vector array. IEEE Trans. Geosci. Remote Sens. 62, 5928210. https://doi.org/10.1109/TGRS.2024.3462435.

Zhao, T., Che, X., Qiao, W., Lu, J., Men, B., Li, G., 2025. 3-D far-field imaging processing algorithm for borehole acoustic reflection imaging utilizing both acoustic pressure and particle velocity. IEEE Trans. Geosci. Remote Sens. 63, 5918115. https://doi.org/10.1109/TGRS.2025.3590750.